260
4-10-80

DR. 1026

MASTER

ornl

ORNL/TM-7142

OAK
RIDGE
NATIONAL
LABORATORY

UNION
CARBIDE

Properties and Structure of CPF8 and CPF8M Centrifugally Cast Pipe

E. Bolling
R. T. King
V. K. Sikka

OPERATED BY
UNION CARBIDE CORPORATION
FOR THE UNITED STATES
DEPARTMENT OF ENERGY

DISCLAIMER

Printed in the United States of America. Available from
the Department of Energy
Technical Information Center
P.O. Box 62, Oak Ridge, Tennessee 37830
Printed Copy A04 ; Microfiche A01

ORNL/TM-7142
Distribution
Categories UC-79h,
-k, -r

Contract No. W-7405-eng-26

METALS AND CERAMICS DIVISION

PROPERTIES AND STRUCTURE OF CPF8 AND CPF8M CENTRIFUGALLY CAST PIPE

E. Bolling, R. T. King, and V. K. Sikka

Date Published: March 1980

NOTICE: This document contains information of preliminary nature. It is subject to revision or correction and therefore does not represent a final report.

OAK RIDGE NATIONAL LABORATORY
Oak Ridge, Tennessee 37830
operated by
UNION CARBIDE CORPORATION
for the
DEPARTMENT OF ENERGY

THIS PAGE

WAS INTENTIONALLY

LEFT BLANK

CONTENTS

PROPERTIES AND STRUCTURE OF CPF8 AND CPF8M CENTRIFUGALLY CAST PIPE*

E. Bolling, R. T. King,† and V. K. Sikka‡

ABSTRACT

The chemical contents, microstructures, tensile properties from room temperature to 649°C, and short-term creep-rupture properties at 538 and 649°C of two CPF8 and two CPF8M cast pipes were investigated. All test specimens had circumferentially oriented tensile axes. One casting of each type had relatively low ferrite content, and one had relatively high ferrite content. The 0.2% yield strength was higher for higher ferrite castings for the entire test temperature range. The ultimate tensile strength was higher for higher ferrite castings only at low temperatures. At 538 and especially 649°C ultimate tensile strength values were not significantly different for the low- and high-ferrite castings. Some of the ultimate tensile strengths were below the minimum values suggested for wrought materials of equivalent compositions. The measured creep-rupture strengths for the cast steels frequently were lower than the suggested minimum values of the wrought counter-parts, types 304 and 316 stainless steel. The creep-rupture ductility of CPF8 material tends to decrease with increasing rupture time at both 538 and 649°C. Fracture at 649°C follows substructural boundaries and is associated with sigma phase formed from the original ferrite phase. The results suggest that separate analyses of the properties of wrought and cast austenitic steels for design are warranted, particularly for elevated-temperature service.

INTRODUCTION

The CPF8 and CPF8M casting grades of stainless steel pipe are the counterparts of wrought types 304 and 316 stainless steel, respectively.

---

*Work performed under DOE/RRT AF 15 10 15, OR-1.3, Mechanical Properties Design Data.

†Present address, Sprague Electric Co., Marshall Street, North Adams, MA 01247.

‡Author to whom inquiries should be addressed.

They are presently accepted for use in nuclear pressure boundary construction under Sect. III of the *ASME Boiler and Pressure Vessel Code*[1] for temperatures below 426°C (800°F).* These cast materials have design stress intensity values at low temperatures that are usually equal to those of their wrought equivalents. Additional safety factors are sometimes applied to castings when they are used for construction in accordance with rules that are less stringent than those of Subsection NB. For example, Class 3 construction (Sect. III, Subsect. ND) employs quality factors from 0.8 to 1.0, depending upon the extent of the nondestructive examination.[2] Even so, the economic advantages of casting parts in their finished geometry or near to it are sufficient to make them competitive. Thus, it is not surprising that castings should be considered for elevated-temperature nuclear service. The economic advantages of castings are probably greatest for intricate or irregular shapes such as pump and valve housings and for some of the internal structural elements, core support structures, and other components that may be welded to the pressure boundary material. In order to develop time-dependent allowable stresses for cast materials, a combination of tensile, fatigue, creep fatigue, and creep data is needed. This article presents limited creep data and some tensile data that have been developed[3] for two CF8 and two CF8M materials that were supplied by a commercial manufacturer.

A particular incentive for carefully examining the properties of cast austenitic steels is the relatively low ductility of certain austenitic welds in long-time creep tests.[4] Ferrite present in welds transforms to sigma phase, and fracture can propagate along the austenite-sigma phase boundaries at total strains in the range from 1 to 5%. Because of the similarities between solidified welds[6] and castings, both of which can have a cellular dendritic grain structure with austenitic subgrains elongated in the solidification direction, cast austenitic steels may exhibit similar behavior. Long-term creep tests provide an indication of this potential problem.

---

*For example, SA-351, Grade CF8 pipe, has design stress intensities of 138 MPa (20 ksi) at 38°C (100°F) and 102 MPa (14.8 ksi) at 426°C (800°F), while SA-375, type 304 stainless steel pipe has design stress intensities of 138 and 105 MPa (20 and 15.2 ksi), respectively.

A final incentive for examining the properties of cast pipe is to provide baseline data for comparison with the properties of wrought products later made from the castings. An ongoing program[7] at ORNL has the goal of demonstrating that cast pipe can be spin-forged or roll-extruded to form large-diameter seamless, wrought pipe for fast breeder reactor applications. The pipes that were characterized in this study were among those used in the cast-and-worked pipe program.

The determination of the properties of centrifugally cast pipe is not straightforward, however. In an earlier study these pipes were found to have highly anisotropic elastic properties,[8] and some preliminary tensile tests showed that the plastic deformation behavior of the castings is also anisotropic.[9] Similar behavior has been observed in a type 308 stainless steel electroslag weld.[6] Particular attention was therefore paid in this study to characterizing the location and orientation of the specimens in the castings. Creep and tensile data presented here are only for one combination of either creep or tensile specimen orientation and location in the pipes, but they were not deliberately selected to emphasize any particular properties of the casting.

PHYSICAL CHARACTERIZATION OF EXPERIMENTAL MATERIAL

Four sections of centrifugally cast pipe were supplied by the Sandusky Foundary and Machine Company, Sandusky, Ohio. Each was 0.589 m OD by 0.486 m ID by 0.61 m long (23.2 by 19.1 by 24 in.). The vendor's characterizations of the materials and ORNL identifications are given in Table 1. To determine whether chemical segregation might have

Table 1. Identification of Centrifugally Cast Pipe

Designation	Pipe Heat	Material	Specimen
CPF8(L)	154344	low ferrite	CC4
CPF8(H)	154345	high ferrite	CC5
CPF8M(L)	154581	low ferrite	CC1
CPF8M(H)	154384	high ferrite	CC8

occurred during solidification, we had spectrographic chemical analyses performed at an industrial laboratory on the inner and outer surfaces of these pipes. The results are given in Table 2. The agreement between the vendor's analyses and the inner and outer surface analyses is quite good. The variations in chemical contents from the inside to the outside are not large compared with normal specification ranges for CPF8 and CPF8M, but there are some consistent trends.

A 0.1-m-long (4-in.) ring was cut from each pipe, and a 100 by 50 by 24-mm slab was sawed from each ring. The slabs were polished on three sides and etched to reveal the macrostructure. (See Figs. 1, 2, and 3). Approximate ferrite numbers (FN) were measured with a Ferritescope on the outer surface of the pipe, the inner surface of the pipe, and points about 5 mm from each surface. These results are compared with ferrite contents calculated by the vendor from the Schaeffler Diagram[10] in Table 3. The variations in ferrite contents from the inner to the outer surfaces of the rings are too large to be explained on the basis of the Schaeffler diagram and must be related to kinetic effects during solidification.

Metallographic sections were cut from each pipe to allow examination of the microstructure through the pipe wall in the planes parallel to and normal to the pipe axis. Sections were also prepared to allow examination of planes just below but parallel to the inner and outer surfaces of the pipe. Since the only differences observed across any section were in the quantity and continuity of the ferrite phase and the change from an elongated to nearly equiaxed structure partway through the CPF8M(H) pipe (see Fig. 2), all micrographs were arbitrarily taken on the outer surface of the pipe (see Figs. 4–7). Examination was performed in the as-polished condition and also after specimens had been etched with Murakami's reagent. The salient features observed in all castings included minor casting porosity, ferrite that qualitatively appears in keeping with the measured ferrite contents listed in Table 3, and a few isolated regions of a phase that is visible in the as-polished condition and may be sigma phase formed by decomposition of the ferrite during cooling of the castings. We did not measure the amounts of the various phases that were present.

Table 2. Comparison of Vendor's Chemical Analysis of Centrifugally Cast Pipe with Spectrographic Analyses Performed on the Inner and Outer Surfaces of the Pipe

Element	Content, wt %, in Pipe by Heat Number and ORNL Pipe Specimen Number					
	Vendor	Inner	Outer	Vendor	Inner	Outer
	CPF8(L)	154344	(CC4)	CPF8(H)	154345	(CC5)
Si	0.92	0.91	0.89	1.48	1.44	1.42
S	0.02	0.019	0.014	0.02	0.019	0.015
P	0.02	0.015	0.012	0.01	0.014	0.013
Mn	1.13	1.13	1.10	0.54	0.58	0.56
C	0.04	0.033	0.021	0.04	0.041	0.033
Cr	19.0	19.05	19.37	20.5	20.63	20.59
Ni	8.5	8.94	8.40	8.5	8.87	8.61
Mo		0.01	0.01		<0.01	<0.01
B		0.002	0.002		0.001	0.001
Nb		<0.01	<0.01		<0.01	<0.01
Ti		<0.01	<0.01		<0.01	<0.01
Co		0.01	0.01		<0.01	<0.01
Cu		0.02	0.02		0.02	0.02
Al		<0.01	<0.01		<0.01	<0.01
V		0.04	0.04		0.05	0.05
N		0.21	0.14		0.16	0.14
	CPF8M(L)	154581	(CC1)	CPF8M(H)	154348	(CC8)
Si	1.00	1.00	0.98	0.98	1.02	1.04
S	0.02	0.022	0.021	0.02	0.024	0.019
P	0.02	0.026	0.025	0.02	0.026	0.027
Mn	1.16	1.12	1.14	1.03	1.03	1.04
C	0.04	0.044	0.039	0.05	0.040	0.034
Cr	19.7	20.20	20.19	20.0	20.47	20.49
Ni	10.2	10.22	10.15	9.2	9.48	9.17
Mo	2.2	2.37	2.35	2.7	2.73	2.70
B		0.002	0.002		0.002	0.002
Nb		<0.01	<0.01		<0.01	<0.01
Ti		0.01	0.01		0.01	0.01
Co	0.04	0.02	0.02	0.03	0.02	0.02
Cu		0.05	0.05		0.06	0.06
Al		0.01	0.01		0.01	<0.01
V		0.05	0.05		0.05	0.05
N		0.17	0.14		0.14	0.11

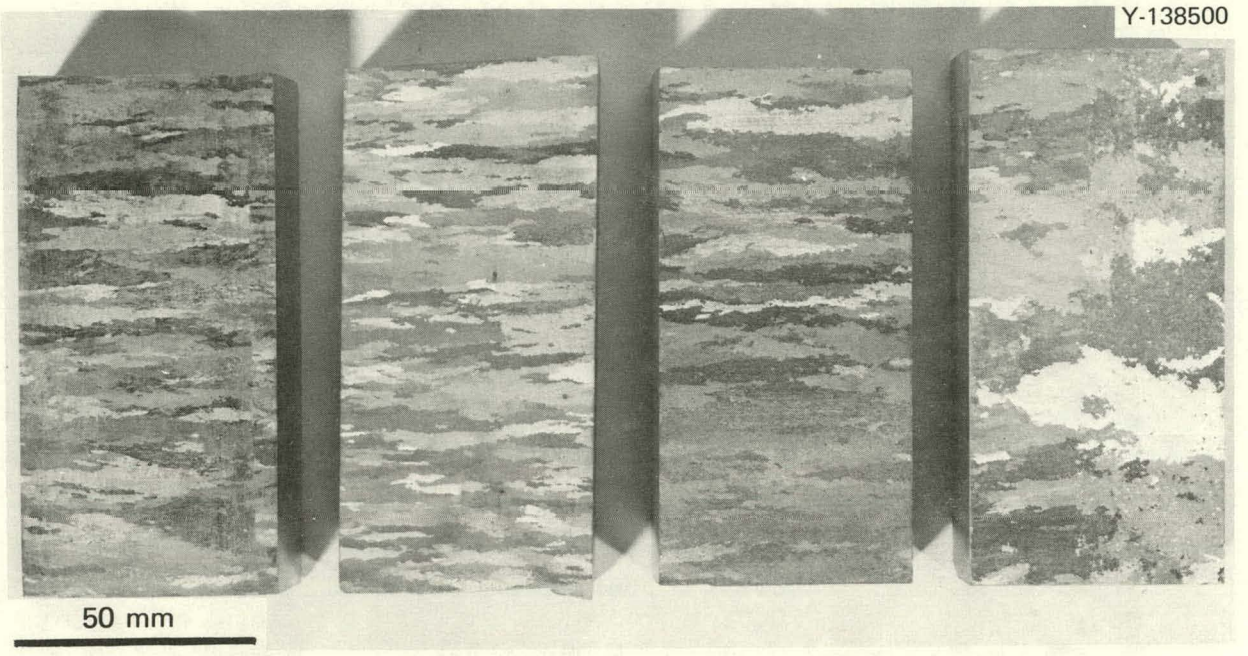

Fig. 1. Macrostructure of Centrifugally Cast Pipes — Radial Section. Left to right: CPF8(L), CPF8(H), and CPF8M(H).

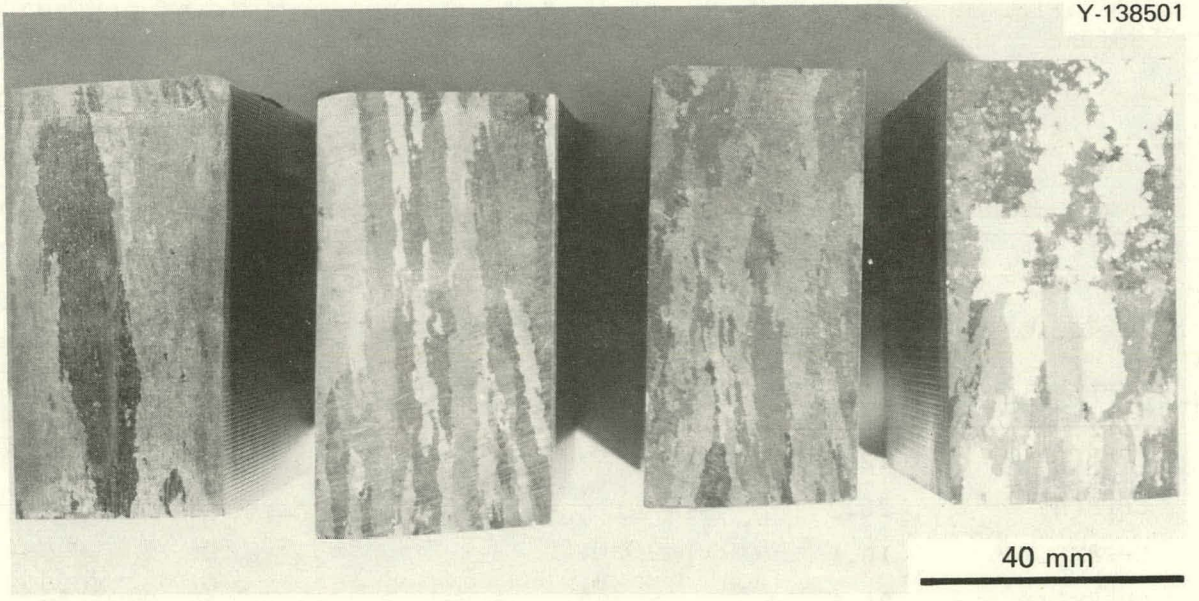

Fig. 2. Macrostructure of Centrifugally Cast Pipes — Section Normal to Pipe Axis. Left to right: CPF8(L), CPF8M(L), CPF8(H), and CPF8M(H).

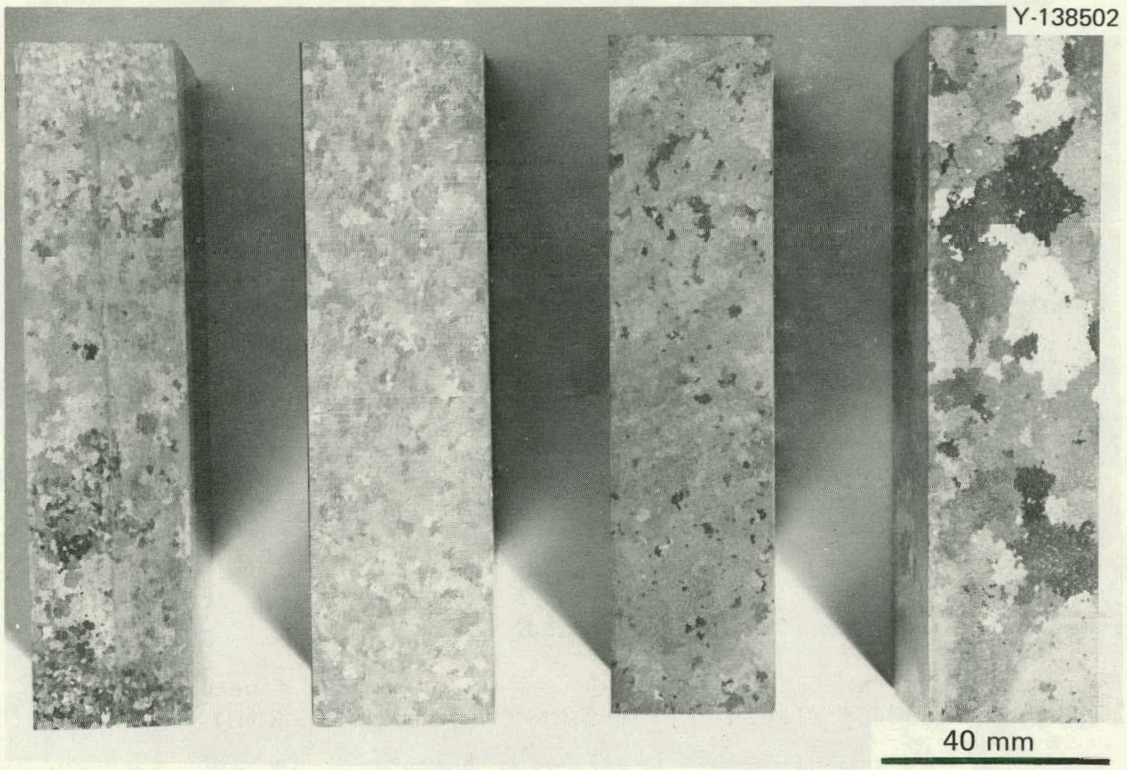

Fig. 3. Macrostructure of Centrifugally Cast Pipes — Outside Surface. Left to right: CPF8(L), CPF8M(L), CPF8(H), and CPF8M(H).

Table 3. Ferrite Numbers and Calculated Ferrite Contents of Centrifugally Cast Pipe

Designation	Calculated Ferrite Content (%)	Measured Ferrite Number (FN)			
		Outside Surface	Inside Surface	5 mm from Outside Surface	5 mm from Inside Surface
CPF8(L)	12.8	1.3	0.5–1.0	0.3–0.3	0.5–1.0
CPF8(H)	26.2	18–20	5–10	10–15	5–10
CPF8M(L)	16.1	10–15	3–5	5–10	5–10
CPF8M(H)	24.5	>30	10–15	20–25	10–15

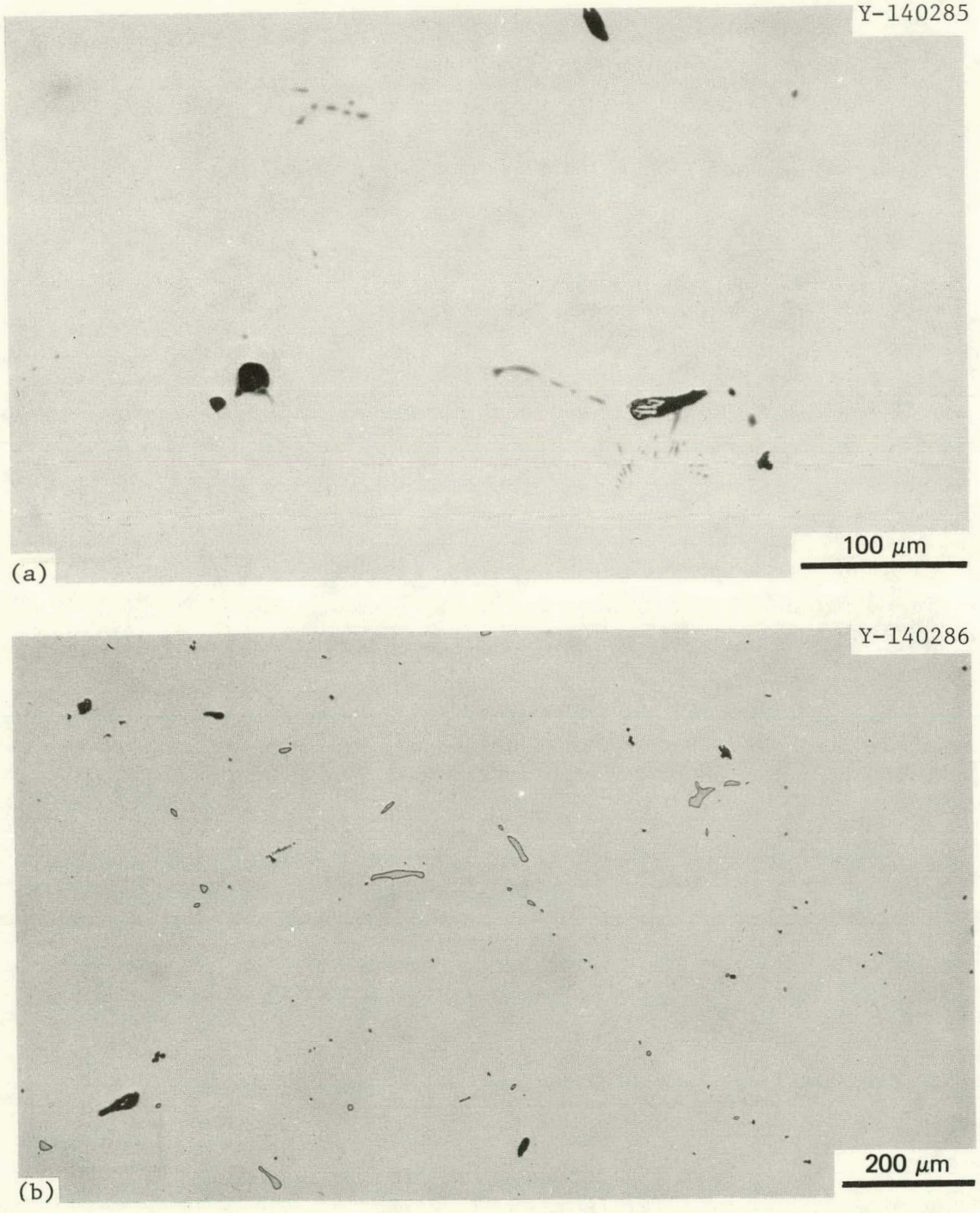

Fig. 4. Microstructure of CPF8(L) Material. (a) As polished, showing second phase and casting voids. (b) Etched with Murakami's reagent showing islands of grey ferrite and black casting voids.

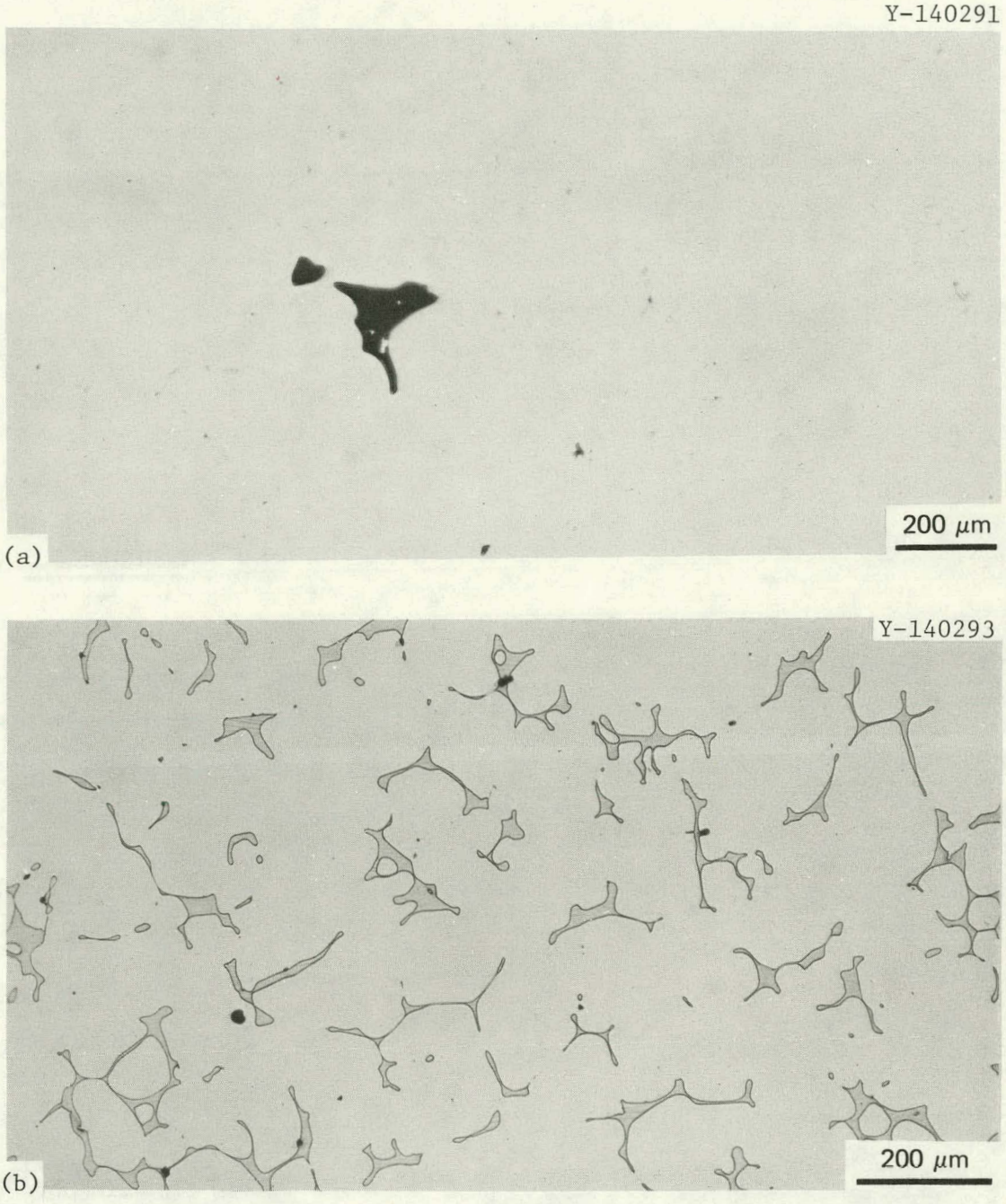

Fig. 5. Microstructure of CPF8(H) Material. (a) As polished, showing casting void with ferrite in light relief. (b) Etched with Murakami's reagent, showing grey ferrite and a few casting voids.

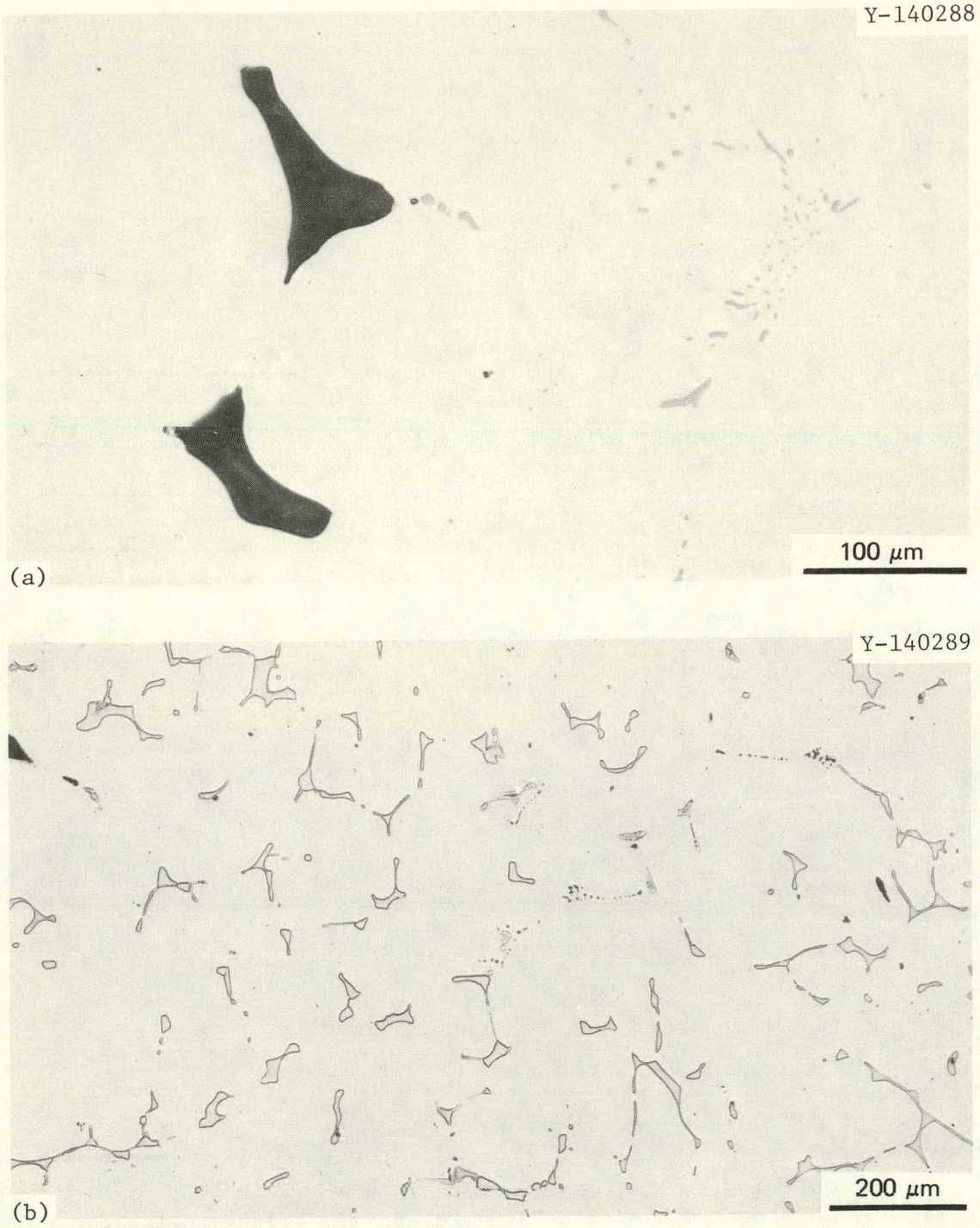

Fig. 6. Microstructure of CPF8M(L) Material. (a) As polished, showing casting porosity and second phase. (b) Etched with Murakami's reagent, showing ferrite, second phase, and same porosity.

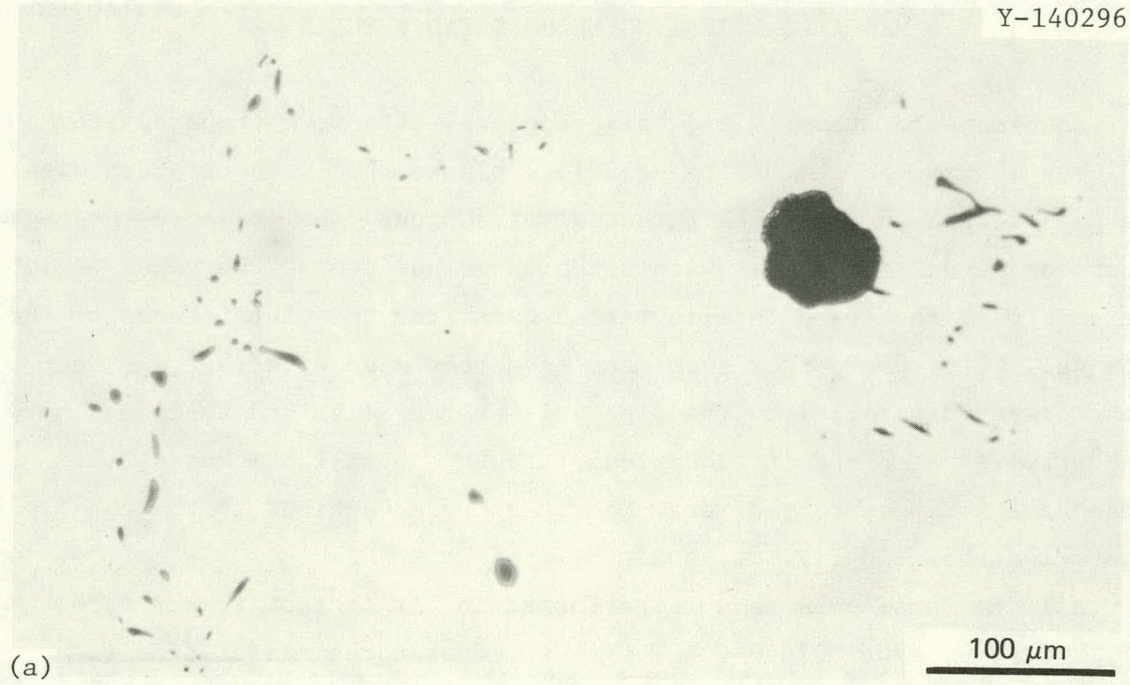

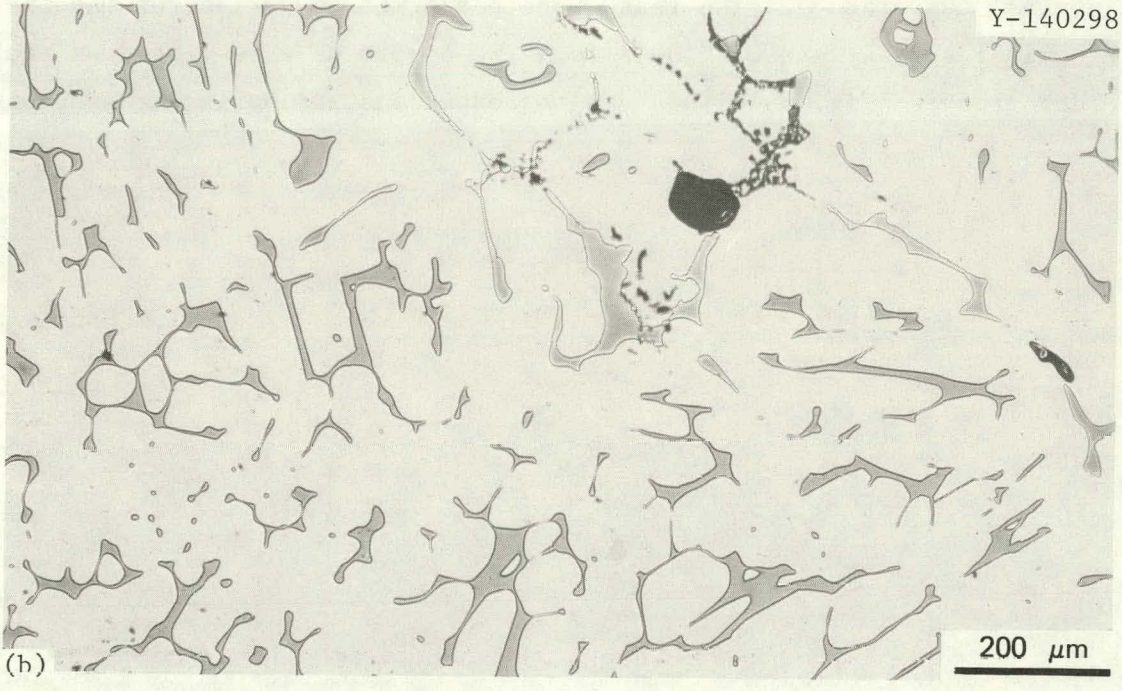

Fig. 7. Microstructure of CPF8M(H) Material. (a) As polished, showing casting porosity and second phase. (b) Etched with Murakami's reagent, showing ferrite, second phase, and porosity.

MECHANICAL TESTING METHODS AND RESULTS

Specimens for tensile and creep-rupture tests were prepared from 16 by 16 by 105-mm (5/8 by 5/8 by 4.13-in.) blanks that were oriented with the gage length in the circumferential direction. The creep-rupture specimens were located just within the outer surface of the pipes while the specimens that were tensile tested came from the midthickness of the pipe wall (Fig. 8). Other specimens have been made with the gage sections oriented parallel to the pipe axis or radially, and specimens have been prepared at different locations through the wall thickness, but these have not been tested yet. Specimens were machined to the configuration shown in Fig. 9.

All the tensile tests were performed in air at room temperature, 100, 200, 300, 538, or 649°C. The test temperatures measured at the top, center, and bottom of the gage section were held within ± 2°C of the nominal temperature. The tests were performed on an Instron machine at a nominal strain rate of 0.004/min. The specimens were fitted on the shoulder grooves (Fig. 9) with averaging extensometers having transducers

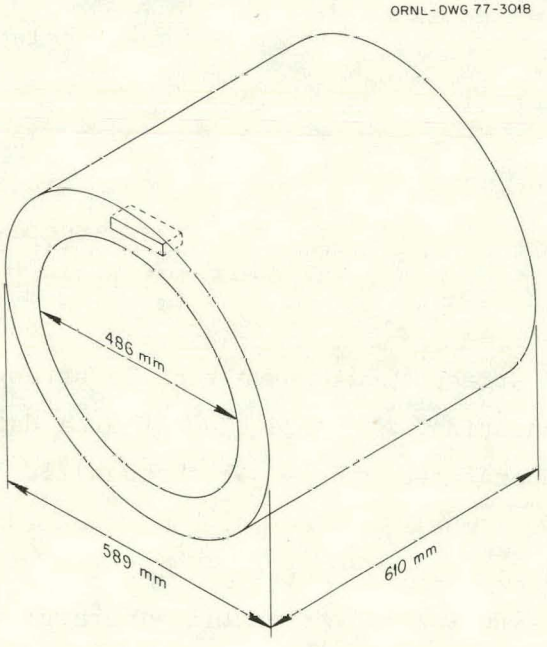

Fig. 8. Location of Specimen Blanks in Centrigually Cast Pipe Sections.

ORNL-DWG 77-3016

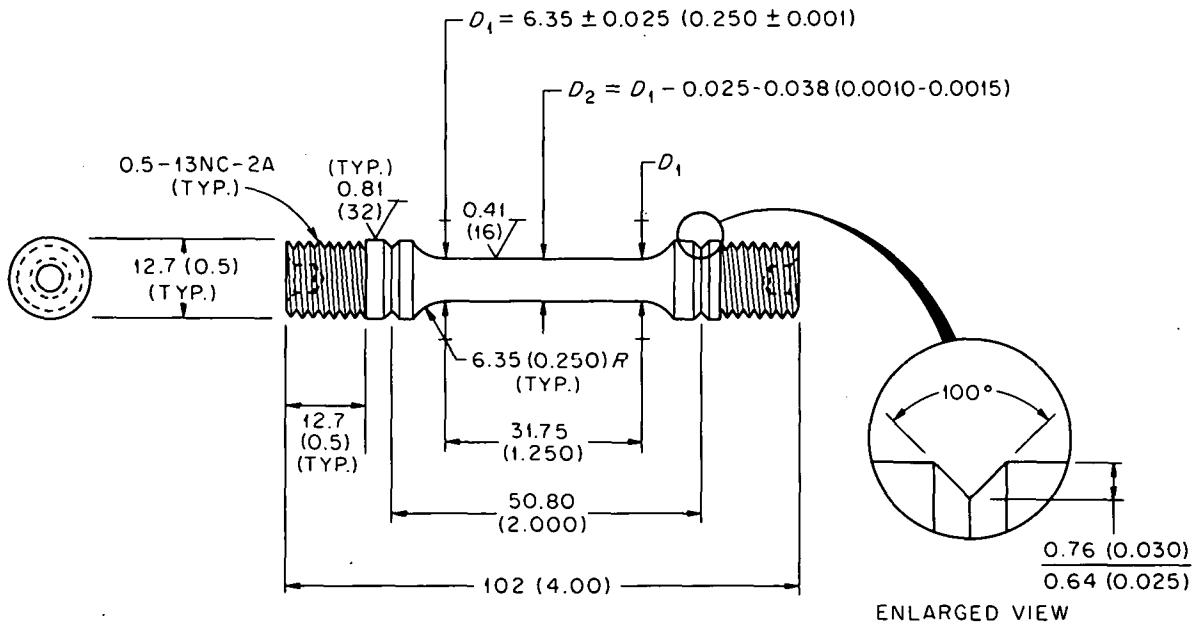

SURFACE FINISHES IN MICROMETERS (MICROINCHES)

DIMENSIONS IN MILLIMETERS (INCHES)

Fig. 9. Design of Creep-Rupture Specimens Prepared from Centrifugally Cast Pipe.

with a 10^{-3} strain sensitivity. A load cell was included in the load train; the signals were used to drive an x-y recorder.

The true stress vs true strain data have been plotted in Figs. 10 and 11 for tests performed at 300°C and below on CPF8 and CPF8M, respectively. The higher ferrite materials have consistently higher strain hardening rates than their lower ferrite counterparts.

The tensile test data for all tests are presented in Tables 4 and 5. The 0.2% offset yield strength, ultimate tensile strength, uniform elongation, total elongation, and reduction of area data are plotted as functions of test temperature in Figs. 12 through 21. Minimum values suggested in the *Nuclear Systems Materials Handbook* (NSMH)[1] for all but the reduction of area are plotted together with the data for the CPF8 and CPF8M castings. Where no values for castings were given in the NSMH, comparisons with suggested minimum values for types 304 and 316 stainless steel were made.

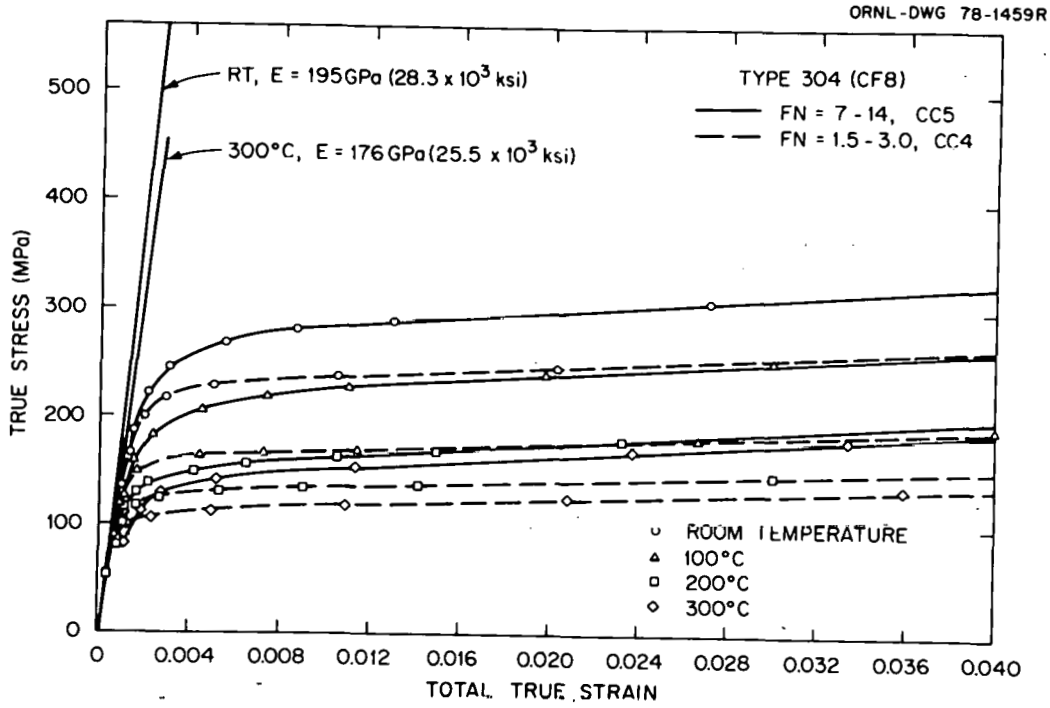

Fig. 10. True Stress-Strain Curves of Centrifugally Cast CPF8 Stainless Steel Showing the Influence of Test Temperature and Ferrite Content.

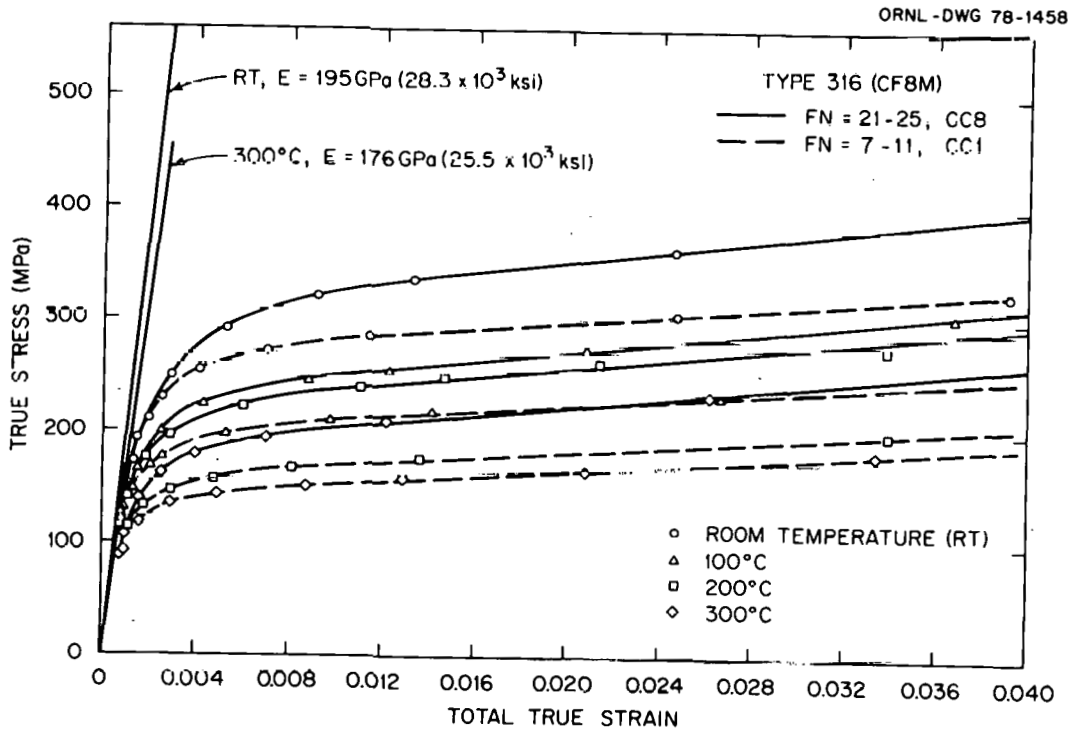

Fig. 11. True Stress-Strain Curves of Centrifugally Cast CPF8M Stainless Steel Showing the Influence of Test Temperature and Ferrite Content.

Table 4. Tensile Test Data for CPF8 Castings CC4 and CC5

Test	Test Temperature		Specimen	Stress, MPa (ksi)				Elongation, %		Reduction of Area (%)
				Proportional Limit	Yield		Tensile	Uniform	Total	
	(°C)	(°F)			0.02%	0.2%				
19,033	25	77	CC4, 32	115(16.7)	180(26.1)	221(32.1)	485(70.4)	44.75	59.25	73.91
19,034	100	212	CC4, 33	57 (8.3)	126(18.3)	160(23.2)	385(55.9)	42.50	63.10	89.60
19,035	200	392	CC4, 34	37 (5.3)	85(12.3)	125(18.2)	356(51.6)	41.81	55.06	75.95[a]
19,036	300	572	CC4, 35	70(10.2)	92(13.3)	108(15.7)	345(50.1)	39.62	51.30	74.52
19,574	538	1000	CC4, 29	34 (4.9)	71(10.3)	94(13.6)	287(41.6)	39.89	47.58	69.01
19,384	538	1000	CC4, 31	41 (5.9)	66 (9.5)	83(12.7)	272(39.5)	46.71	58.68	69.01
19,385	649	1200	CC4, 36	34 (4.9)	66 (9.6)	83(12.1)	208(30.2)	26.27	33.46	34.33
19,037	25	77	CC5, 31	134(19.4)	201(29.2)	257(37.3)	544(78.9)	56.50	66.60	82.07
19,038	100	212	CC5, 32	72(10.5	139(20.2)	197(28.5)	460(66.7)	39.20	51.10	72.68
19,039	200	392	CC5, 33	71(10.3)	113(16.4)	145(21.0)	410(59.5)	38.09	46.85	79.15
19,040	300	572	CC5, 34	68 (9.8)	103(14.9)	137(19.9)	401(58.1)	40.35	46.50	72.31
19,386	538	1000	CC5, 35	57 (8.2)	89(12.9)	117(16.9)	325(47.2)	41.75	51.23	55.90
19,387	649	1200	CC5, 36	48 (6.9)	75(10.9)	102(14.8)	222(32.2)	22.82	26.15	27.60

[a]Specimen measured separately.

Table 5. Tensile Test Data for CPF8M Castings CC1 and CC8

Test	Test Temperature (°C)	Test Temperature (°F)	Specimen	Stress, MPa (ksi) Proportional Limit	Yield 0.02%	Yield 0.2%	Tensile	Elongation, % Uniform	Elongation, % Total	Reduction of Area (%)
19,029	25	77	CC1, 31	77(11.1)	168(24.3)	244(35.4)	532(77.1)	54.74	69.70	78.82
19,030	100	212	CC1, 32	82(11.9)	141(20.5)	185(26.8)	441(64.0)	38.04	46.45	85.49
19,031	200	392	CC1, 33	84(12.2)	118(17.1)	150(21.8)	403(58.4)	34.46	43.13	60.81
19,032	300	572	CC1, 34	53 (7.7)	107(15.5)	136(19.7)	387(56.1)	32.60	39.82	68.77
19,382	538	1000	CC1, 35	59 (8.5)	87(12.6)	122(17.7)	345(50.0)	42.22	50.38	77.41
19,383	649	1200	CC1, 36	46 (6.7)	80(11.6)	110(15.9)	241(35.0)	33.09	40.07	45.37
19,041	25	77	CC8, 31	103(14.9)	179(26.0)	272(39.5)	554(80.3)	35.26	42.04	87.05
19,042	100	212	CC8, 32	101(14.6)	157(22.7)	188(27.2)	463(67.1)	30.00	44.90	87.23
19,043	200	392	CC8, 33	81(11.8)	126(18.3)	200(29.0)	489(70.9)	24.61	34.25	59.04
19,044	300	512	CC8, 34	73(10.6)	118(17.1)	174(25.3)	467(67.8)	36.30	39.07	37.21[a]
19,388	538	1000	CC8, 35	61 (8.9)	110(16.0)	150(21.7)	372(54.0)	35.82	32.87	55.05
19,389	649	1200	CC8, 36	48 (6.9)	84(12.2)	130(18.9)	237(34.4)	27.36	37.74	54.43

[a]Specimen measured separately.

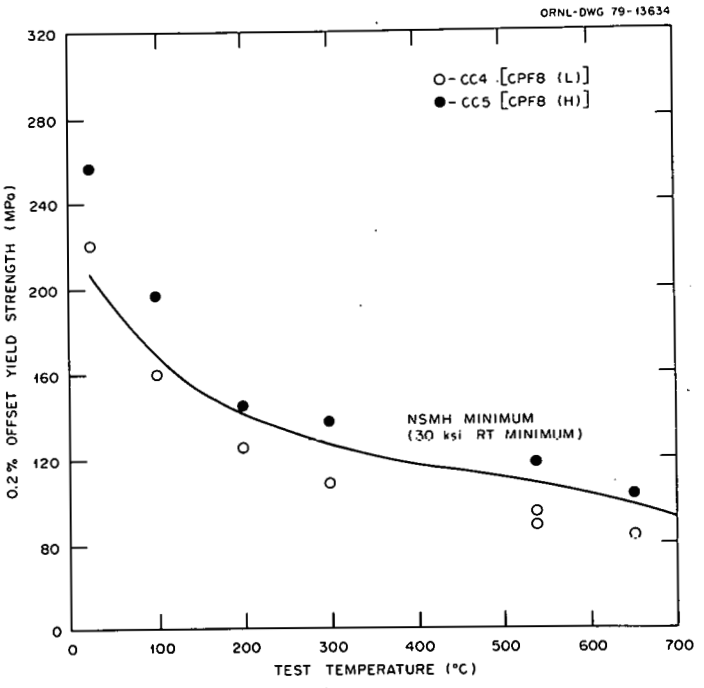

Fig. 12. The 0.2% Offset Yield Strength of CPF8 Castings.

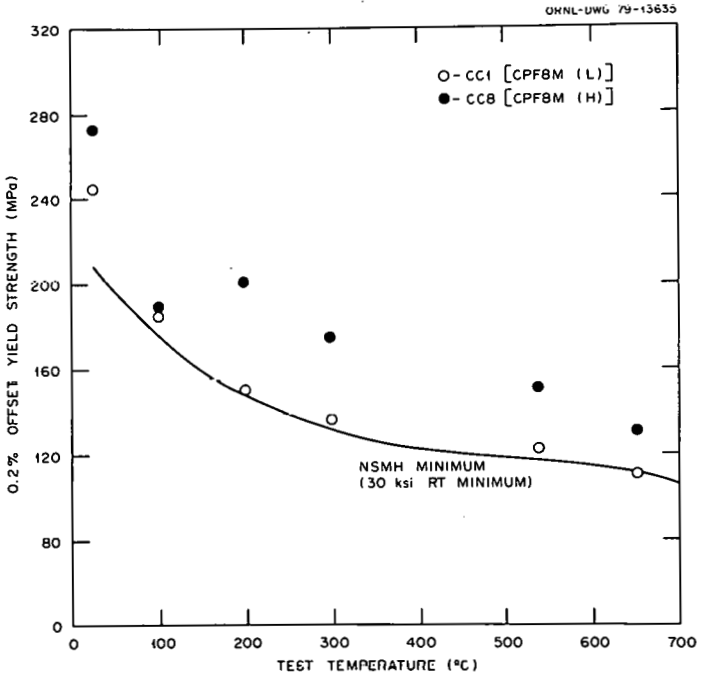

Fig. 13. The 0.2% Offset Yield Strength of CPF8M Castings.

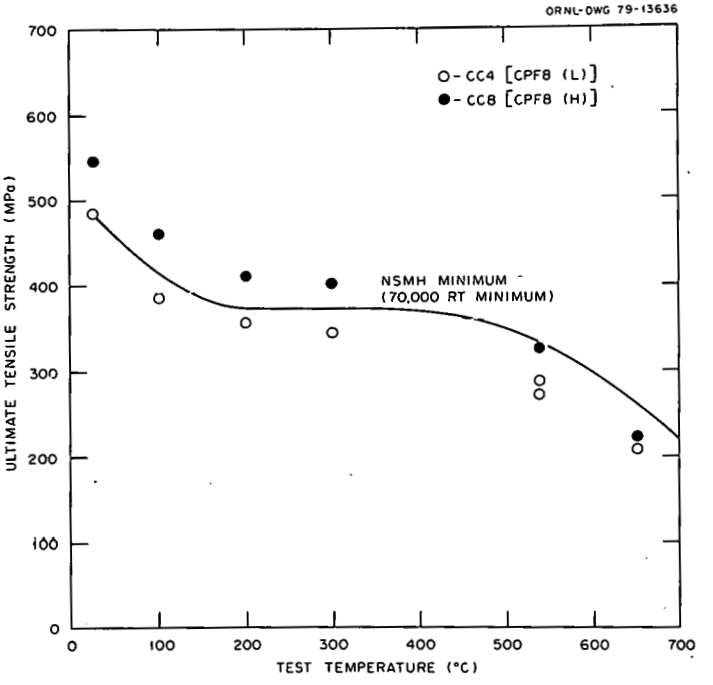

Fig. 14. Ultimate Tensile Strength of CPF8 Castings.

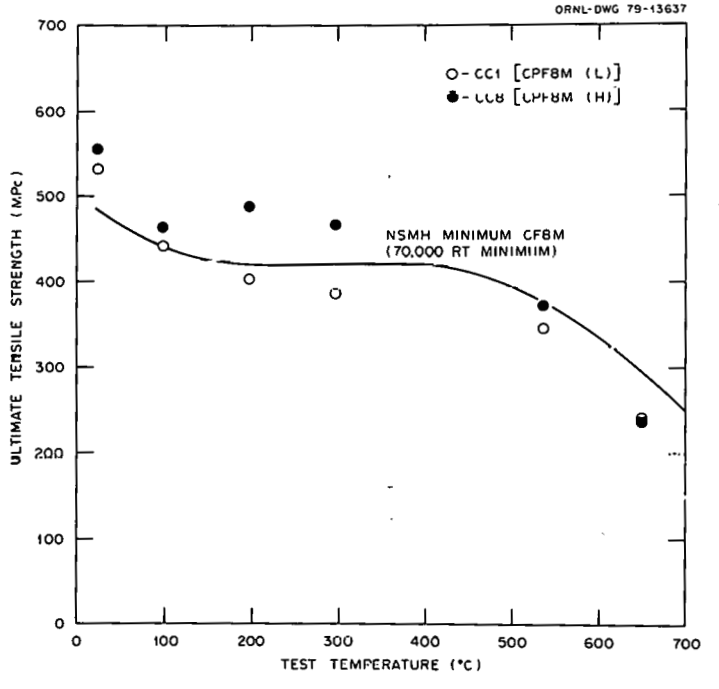

Fig. 15. Ultimate Tensile Strength of CPF8M Castings.

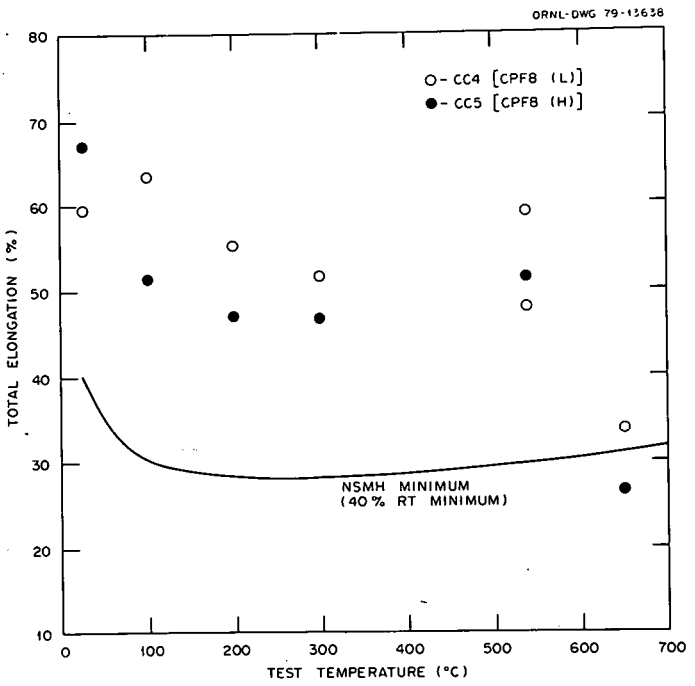

Fig. 16. Total Tensile Elongation of CPF8 Castings.

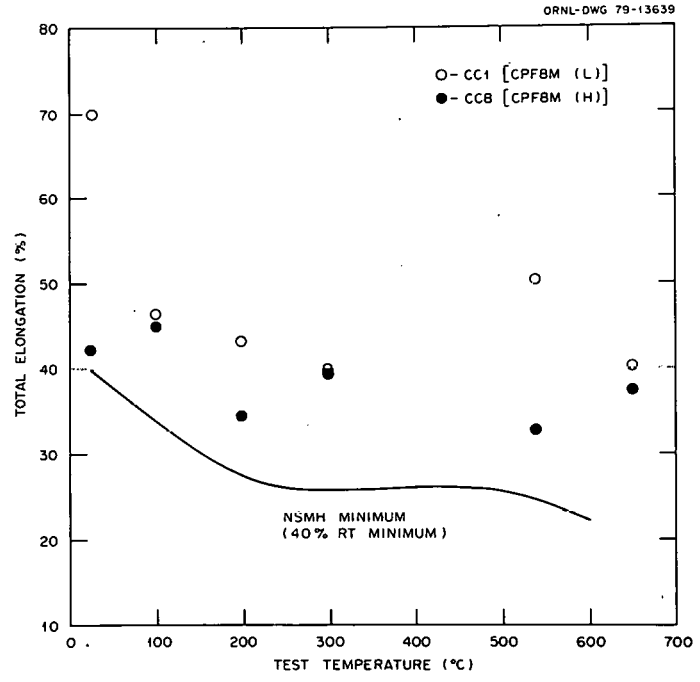

Fig. 17. Total Tensile Elongation of CPF8M Castings.

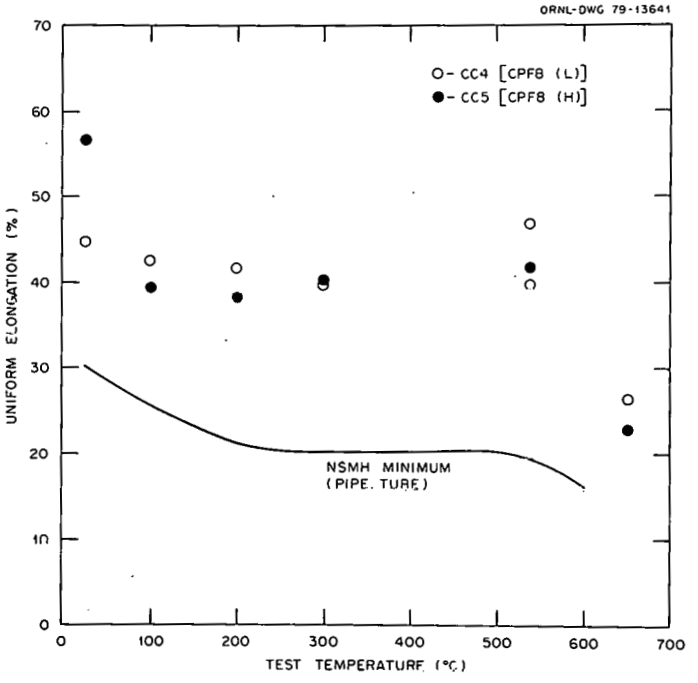

Fig. 18. Uniform Elongation of CPF8 Castings.

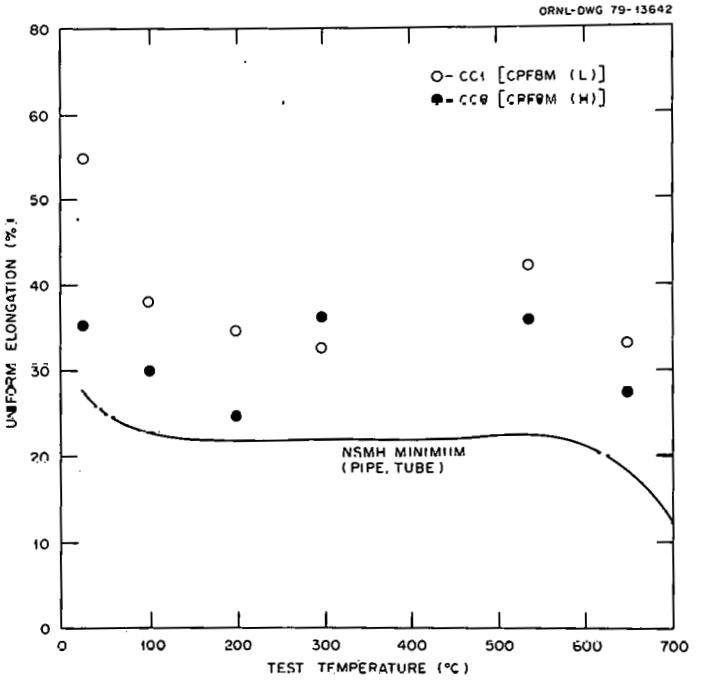

Fig. 19. Uniform Elongation of CPF8M Castings.

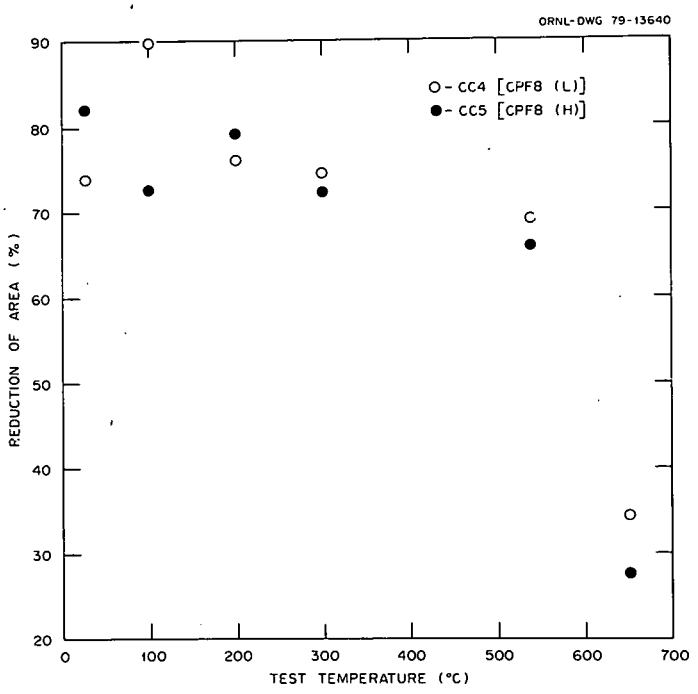

Fig. 20. Tensile Reduction of Area of CPF8 Castings.

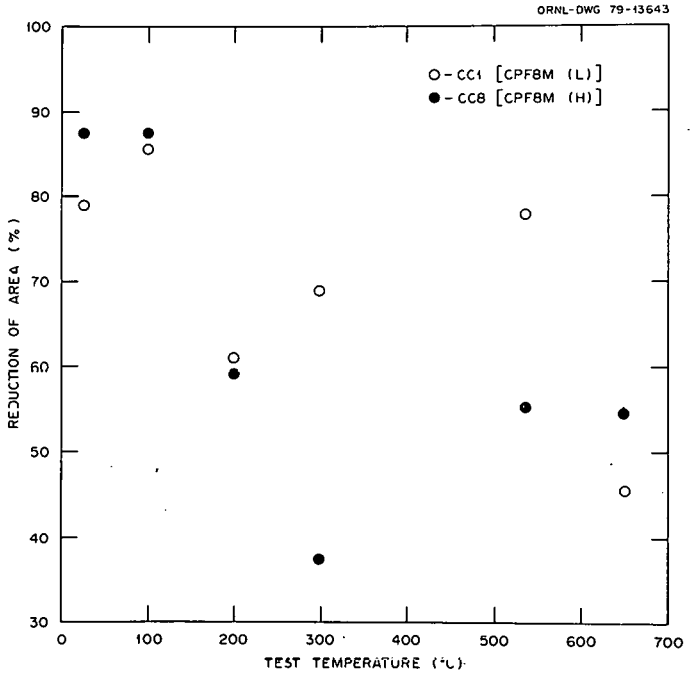

Fig. 21. Tensile Reduction of Area of CPF8M Castings.

The significant findings include these points:

1. The higher ferrite CPF8 and CPF8M castings have consistently higher yield and ultimate tensile strengths than their lower ferrite counterparts (Figs. 12–15). However, the difference in ultimate tensile strength for the two ferrite contents diminishes at 538 and 649°C.

2. The yield strength and ultimate tensile strength of the low-ferrite CPF8 are consistently below the minimum values suggested by the NSMH[11] for wrought material. The increase in yield strength with ferrite content agrees with the findings of other workers.[12]

3. At elevated temperatures, particularly 538 and 649°C, the ultimate tensile strengths of all the castings fell below the minimum values suggested by the NSMH for wrought material.

4. The total elongations and uniform elongations of the castings were all higher than the minimum values suggested by the NSMH wrought material except for one datum — the total elongation of high-ferrite CPF8 at 649°C (Figs. 16–19).

5. Reductions of area tended to exceed 40% except for CPF8 at 649°C (Figs. 20–21).

All the creep tests were performed in air at nominal temperatures of 538 and 649°C (1000 or 1200°F). The temperatures measured at the top, center, and bottom of the gage were held within ± 2°C (4°F) of the nominal temperature. All loads were applied gradually and smoothly by manually lowering a jack to produce a strain rate during loading of about 0.004/min. Strains during loading and the first few hours of testing were usually recorded continuously from an averaging extensometer mounted on the shoulders of the specimens. The stresses were selected to produce rupture times in the range from 1 to about 1000 h.

The creep and creep rupture data are summarized in Tables 6 and 7. The times to several important events during creep testing, including the end of primary or first-stage creep, the end of second-stage creep by departure from linearity, and the onset of tertiary creep as determined by a 0.2% offset line from second-stage creep were obtained by visual estimates from the strain-time curves, as were the strains at these events. Times to various strains were obtained by linear interpolation between the nearest strain-time data pairs. The fraction of

Table 6. Creep Strain Data for CPF8 and CPF8M Centrifugally Cast Pipe at 538 and 649°C (1000 and 1200°F)

Alloy	Casting	Stress		Strain, %, for Each Stage							Reduction of Area (%)	$\epsilon_{III}/\epsilon_r$		Minimum Strain Rate, %/h	
		(MPa)	(ksi)	Loading	First	Second, Linearity	Second, Offset	Third, Linearity	Tertiary Offset	Total		Total	Creep	Linearity	Offset
							Properties at 538°C (1000°F)								
CPF8	CC4	310	45.0							47.1	49.9				
		291	35.0	22.9	0.12	1.3	1.5	5.8	5.6	30.1	34.3	0.81	0.22	0.0161	0.0183
		96.5	14.0	1.48						>3.6					
CPF8	CC5	276	40.0	22.8	1.0	5.8	6.0	4.0	3.8	33.6	28.5	0.89	0.65	0.364	0.376
		241	35.0	16.7	3.1	1.5	2.4	5.4	4.5	26.7	26.3	0.83	0.55	0.061	0.0694
CPF8M	CC1	310	45.0	24.0	3.3	1.2	1.6	6.2	5.7	34.6	42.1	0.84	0.46	0.0077	0.0084
		276	40.0	20.7	1.7	2.6	3.0	5.5	5.1	30.6	28.0	0.83	0.48	0.0022	0.0023
CPF8M	CC8	310	45.0	17.3	2.4	1.8	2.5	5.7	5.0	27.2	34.7	0.82	0.49	0.0062	0.0068
		276	40.0	17.9	2.6	1.7	2.2	12.0	11.5	34.2	47.3	0.66	0.29	0.0038	0.0041
							Properties at 649°C (1200°F)								
CPF8	CC4	172	25.0	13.4	2.0	1.1	1.6	8.4	7.9	24.9	33.9	0.68	0.31	0.161	0.116
		124	18.0	8.0	1.3	0.6	0.9	7.7	6.8	17.0	20.4	0.60	0.24	0.0090	0.0106
		124	18.0	4.4	7.4	0.9	1.0	6.5	6.4	13.1	20.6	0.51	0.28	0.0093	0.010
CPF8	CC5	172	25.0	10.4	2.6	0.8	1.1	3.9	3.5	17.6	23.0	0.80	0.51	1.3	1.6
		124	18.0	3.2	2.8	0.9	1.2	6.0	5.8	13.0	12.4	0.55	0.41	0.0462	0.0566
		124	18.0	1.7	2.4	1.1	1.5	13.2	12.8	18.4	9.2	0.30	0.23	0.031	0.034
		97	14.0	0.9	0.4	1.0	1.7	4.5	3.9	6.9	8.4	0.44	0.31	0.0042	0.0047
CPF8M	CC1	172	25.0	6.2	7.1	3.1	4.3	3.9	2.7	20.2	23.9	0.86	0.56	0.111	0.121
		172	25.0	8.7	6.4	2.5	3.8	6.2	4.9	23.8	21.9	0.79	0.68	0.118	0.125
		124	18.0	0.86	3.8	5.1	6.5	10.9	9.5	20.6	19.4	0.54	0.52	0.006	0.0061
CPF8M	CC8	172	25.0	5.1	6.7	2.2	3.1	4.3	3.4	18.3	29.5	0.81	0.49	0.32	0.35
		172	25.0	3.6	10.3	3.1	4.6	4.6	3.0	21.5	26.5	0.86	0.83	0.170	0.180
		124	18.0	0.6	6.6	2.8	5.0	6.7	4.5	16.6	22.6	0.73	0.72	0.0092	0.0099

Table 7. Creep Test Time Data for CPF8 and CPF8, Centrifugally Cast Pipe at 538 and 649°C (1000 and 1200°F)

Alloy	Casting	Stress (MPa)	Stress (ksi)	Time to Various Events, h: End of Stage First	End of Stage Second	t_{III}[a]	t_r, Rupture	Creep Strain of 0.5%	Creep Strain of 1%	Creep Strain of 2%	Diametral Strain Ratio: At Fracture	Diametral Strain Ratio: Away From Fracture	$\frac{t_{III}}{t_r}$
Properties at 538°C (1000°F)													
CPF8(L)	CC4	310	45.0				∿0.01				1.6		
		241	35.0	3.6	83.6	35.0	102.8	23.1	59.6	87.2	2.8	3.6	0.83
		96.5	14.0[b]				>12,328.4	20.2	2560.0	∿11,000			
CPF8(H)	CC5	276	40.0	0.2	16.0	16.1	16.4	0.14	0.2	2.7	3.5	3.2	0.98
		241	35.0	19.8	44.3	54.0	58.2	0.4	1.2	7.4	2.5	3.0	0.93
CPF8M(L)	CC1	310	45.0	13.9	299.2	331.2	502.8	4.2	7.0	30.1	2.0	2.9	0.66
		276	40.0	20.0	135.0	149.0	1812.4	8.5	26.7	32.5	4.4	5.1	0.82
CPF8M(H)	CC8	310	45.0	51.8	341.2	426.3	502.4	4.7	6.7	22.0	6.3	2.4	0.85
		276	40.0	100.0	539.8	627.5	971.4	4.8	8.1	27.4	5.7	5.6	0.65
Properties at 649°C (1200°F)													
CPF8(L)	CC4	172	25.0	6	13	15.5	18.2	0.7	2.3	6.5	8.2	4.6	0.85
		124	18.0	66.6	129.5	153.7	158.1	12.7	50.7	141.4	4.8	14	0.97
		124	18.0	65.7	161.3	163.0	167.2	7.2	32.7	135.3	2.5	1.0	0.97
CPF8(H)	CC5	172	25.0	0.7	1.3	1.4	1.5	0.04	0.1	0.4	2.1		0.93
		124	18.0	12.8	33.2	3.4	34.8	0.1	0.3	3.8	4.2	9.2	0.98
		124	18.0	15.4	52.23	60.5	61.8	0.01	0.4	6.9	2.2	2.4	0.98
		96.5	14.0	12.5	262	387	407.1	40.0	172.0	374.0	1.5	2.8	0.95
CPF8M(L)	CC1	172	25.0	15.8	44.5	51.0	51.5	∿0.01	∿0.01	∿0.01	5.6	3.2	0.99
		172	25.0	19.4	40.5	49.9	53.8	0.07	0.15	0.06	2.4		0.93
		124	18.0	347.0	1275.9	140.4	2214.5	0.9	6.7	80.0	3.5	5.6	0.63
CPF8M(H)	CC8	172	25.0	5.1	12.0	14.0	16.4	0.013	0.016	0.019	3.3	1.7	0.85
		172	25.0	24.4	42.5	50.1	53.1	0.02	0.09	0.2	1.3		0.94
		124	18.0	299.7	603.2	804.5	916.3	0.15[c]	0.5[c]	3.9[c]	2.0	2.0	0.88

[a] 0.2% offset to onset of tertiary creep.

[b] Test discontinued after 12,328.4 h.

[c] 0.15 h to 1% total strain, 1.3 h to 2% total strain.

the creep test time before the onset of tertiary creep (t_{III}/t_r), the fraction of total strain before the onset of tertiary creep ($\varepsilon_{III}/\varepsilon_r$, total), and the fraction of creep strain before the onset of tertiary creep ($\varepsilon_{III}/\varepsilon_r$, creep) were computed from these data. The reduction of area was computed on the assumption that the measured maximum and minimum diameters at rupture were the major and minor axes of an elliptical projected fracture surface. The minimum strain rate was calculated both for a line drawn through the second-stage creep data and for a line joining the point at which second-stage creep began with the point of the onset of tertiary creep by the 0.2% offset method. The maximum and minimum diameters of the oval specimens were measured at the point of fracture and at an arbitrarily selected plane at least 5 mm from the fracture. The ratio of diametral strains in either plane is a rough guide to the anisotropy of deformation. Because the surfaces of the tested specimens are irregular as a result of the large grain sizes of the materials, the numbers are only representative and are not very reproducible.

Several noteworthy observations for the creep data follow.

1. The rupture times measured here for both CPF8 and CPF8M are generally shorter than those expected for the respective equivalent wrought grades. The lower halves of the scatter bands for wrought material at 538 and 649°C (1000 and 1200°F) are shown in Figs. 22 and 23. These bands were defined as the regions between average stress rupture curves and the (P = 0.90, γ = 0.95) lower tolerance limit for type 304 stainless steel,[13] and the region between average curves and those curves displaced by −1.65 standard deviations for type 316 stainless steel.[14] In nearly all cases, the cast metal data occur low in or below the scatter bands thus defined.

2. The CPF8(L) casting CC4, which had FN of 0.3 to 3.3 in the same region as the specimen gage length, was significantly stronger than CPF8(H) casting CC5 with FN from 10 to 15. However, the CPF8M castings CC1 and CC8, with FN ranges 5 to 10 and 20 to 25, had virtually identical strengths. Further work is needed to determine whether ferrite, which has a strengthening effect on room-temperature tensile properties,

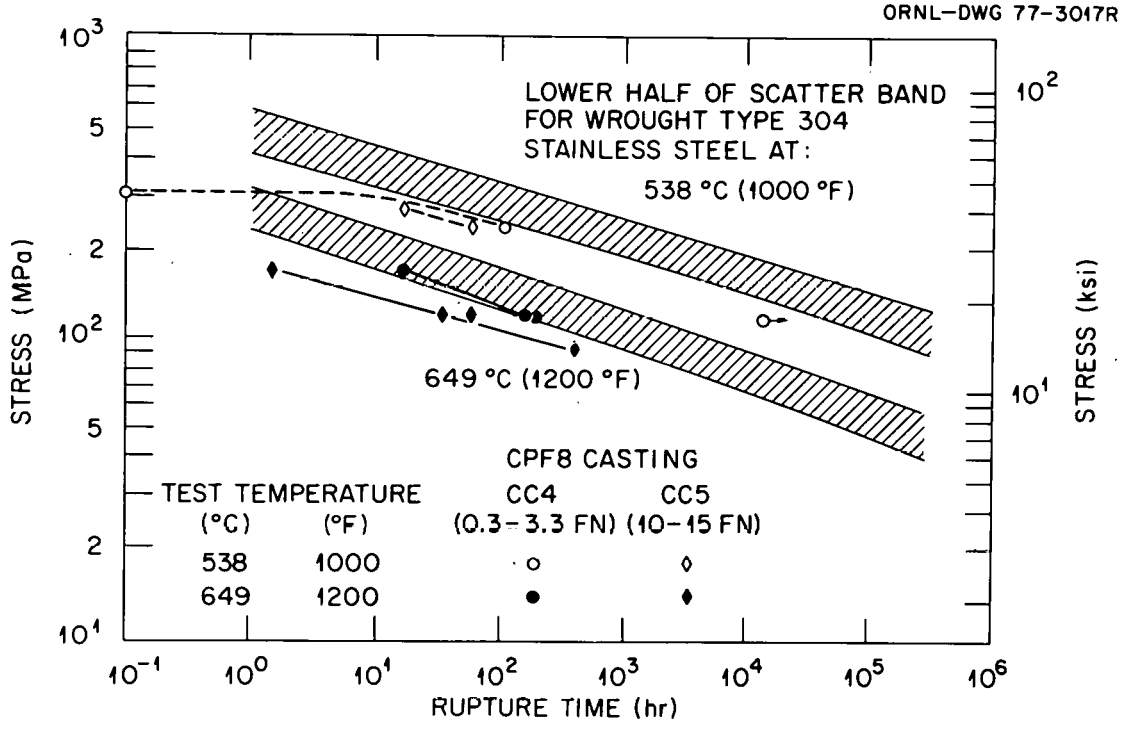

Fig. 22. Comparisons of the Creep-Rupture Properties of CPF8 Castings and Wrought Type 304 Stainless Steel at 538 and 649°C (1000 and 1200°F).

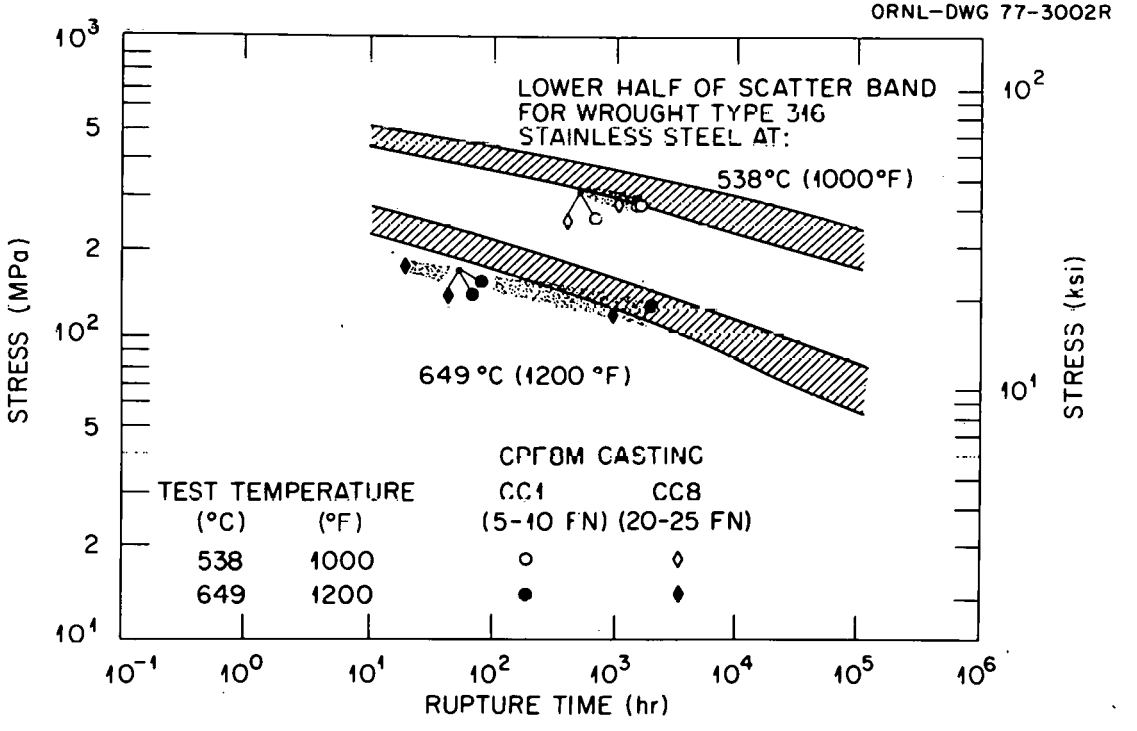

Fig. 23. Comparison of the Creep-Rupture Properties of CPF8M Castings and Wrought Type 316 Stainless Steel at 538 and 649°C (1000 and 1200°F).

is desirable from the standpoint of creep strength. Meaningful conclusions cannot be drawn from these limited results because of other influencing variables.

3. The total strain at rupture and reduction of area of CPF8 decrease with increasing rupture time at both 538 and 649°C (see Fig. 24). These measures of ductility for CPF8M did not exhibit any clear trends (Fig. 25). However, the ductilities measured at 538°C tended to be higher than those measured at 649°C for both materials.

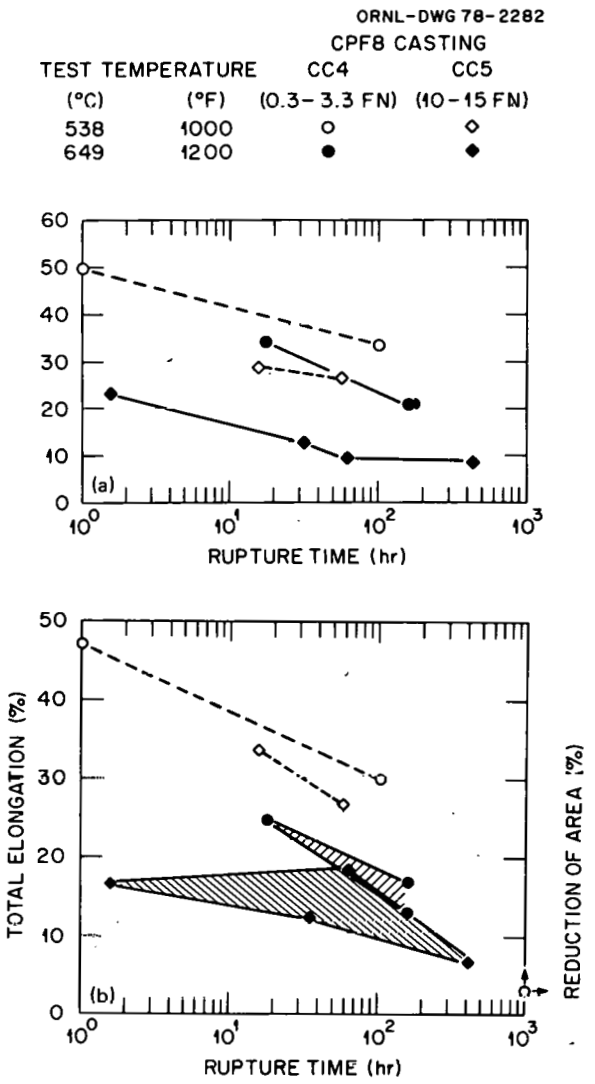

Fig. 24. Creep-Rupture Ductility of CPF8 Castings at 538 and 649°C (1000 and 1200°F). (a) Total strain. (b) Reduction of area.

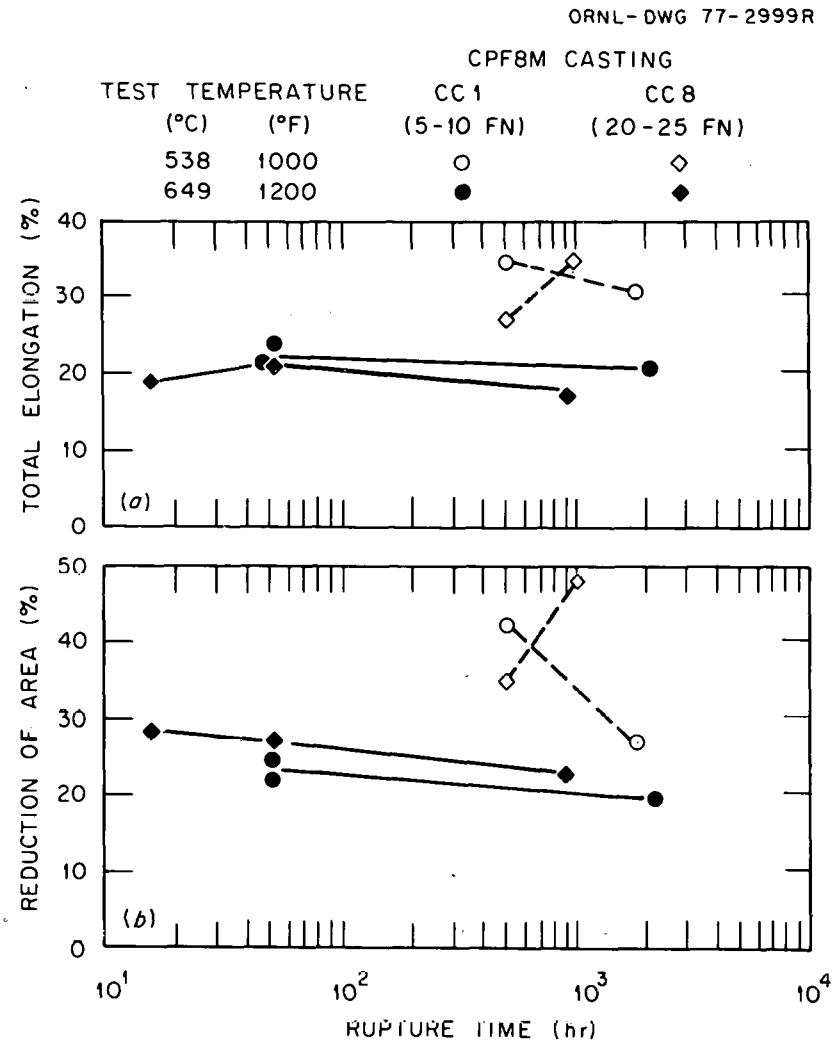

Fig. 25. Creep-Rupture Ductility of CPF8M Castings at 538 and 649°C (1000 and 1200°F). (a) Total strain. (b) Reduction of area.

4. Disregarding plastic strain during loading, the creep component of strain to rupture for CPF8 is in the range of 6 to 17% (Fig. 26), while that for CPF8M is in the range from 9 to 20% (Fig. 27).

5. Usually creep specimens are in first- and second-stage creep for more than 0.8 of their total test time (see t_{III}/t_r in Table 7).

6. Over half the total strain usually occurs before the onset of tertiary creep (see $\varepsilon_{III}/\varepsilon_r$, total, in Table 6).

7. Creep strain before tertiary creep ranges from 0.2 to 0.8 times creep strain to rupture (deleting plastic loading strain).

The reader should recognize the preliminary and somewhat scanty nature of these data and not attempt unwarranted extrapolations.

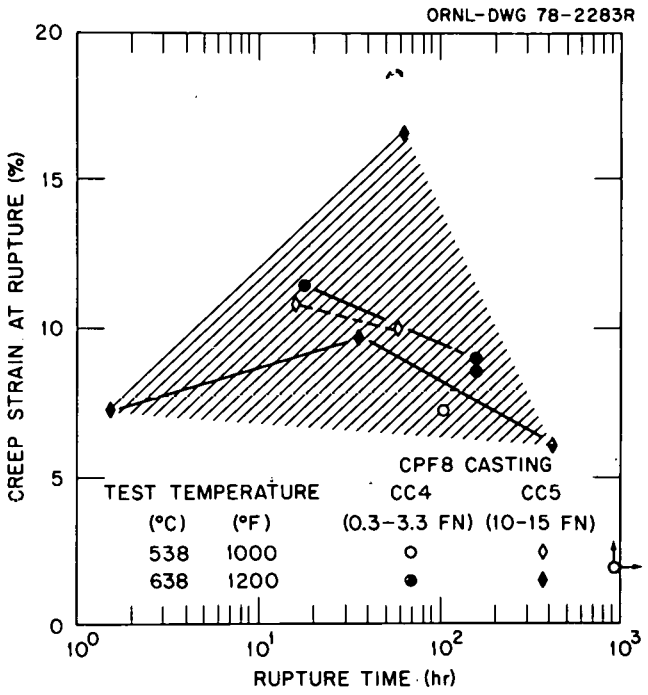

Fig. 26. Creep Strain to Rupture of CPF8 Castings at 538 and 649°C (1000 and 1200°F).

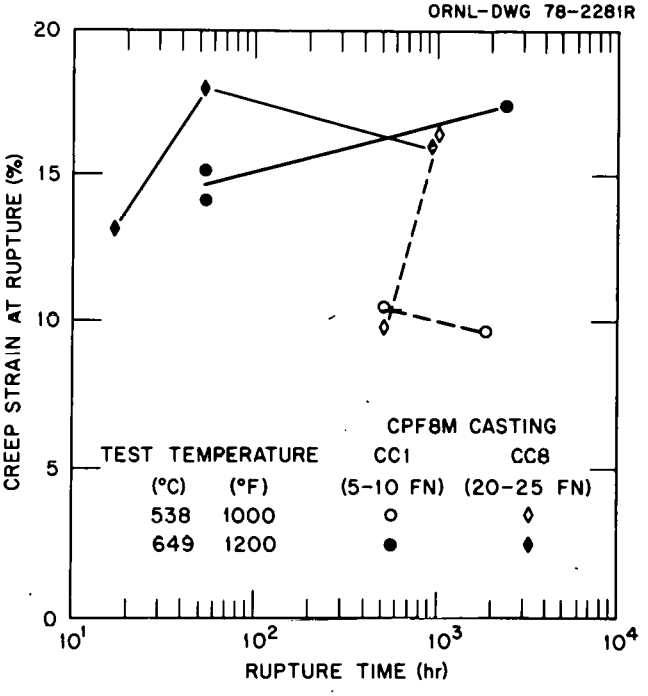

Fig. 27. Creep Strain to Rupture of CPF8M Castings at 538 and 649°C (1000 and 1200°F).

METALLOGRAPHIC OBSERVATIONS ON TESTED SPECIMENS

Because such data are rare in the literature, we have included an extensive set of metallographic observations on creep-rupture-tested specimens in this report.

The mode of failure in creep rupture of each heat of pipe was explored for one sample tested at 538°C and one specimen tested at 649°C. One half of each tested specimen was sectioned to view the plane of the major axis of the elliptical fracture surface and the plane of the minor axis. After they were mounted and polished, the sections were etched with modified Murakami's reagent[16] to reveal the distribution of ferrite and sigma phase in the gage section near the fracture. The optical microstructures are shown in Figs. 28 through 35. The most significant observations are:

1. The CPF8(L) and CPF8(H) materials tested at 538°C did not exhibit extensive transformation of ferrite, although at 1500× some transformation products may be visible at the austenite-ferrite boundaries (Figs. 28, 30).

2. In the CPF8M(L) and CPF8M(H) materials tested at 538°C, the ferrite appears to have partially transformed, but the products cannot be resolved at 1500× (Figs. 32, 34).

3. Ferrite transformed extensively to sigma phase for all material tested at 649°C (Figs. 29, 31, 33, and 35). The transformation appeared to involve nucleation of sigma phase at many sites within a single region of ferrite, as has been reported before.[15]

4. For all materials tested at 538°C, the fracture tended to follow the ferrite phase, and for all materials tested at 649°C, the fractures tended to follow the transformed ferrite regions. Because ferritic steels are generally weaker than austenitic steels for these testing conditions, it is tempting to hypothesize that the presence of a nearly continuous ferrite phase causes the relatively low creep-rupture strengths of these cast steels. Indeed, the low-ferrite CPF8 material (CC4) is stronger than the higher ferrite CPF8 material (CC5) (see Fig. 10). However, these data are influenced by too many other variables to justify firm conclusions.

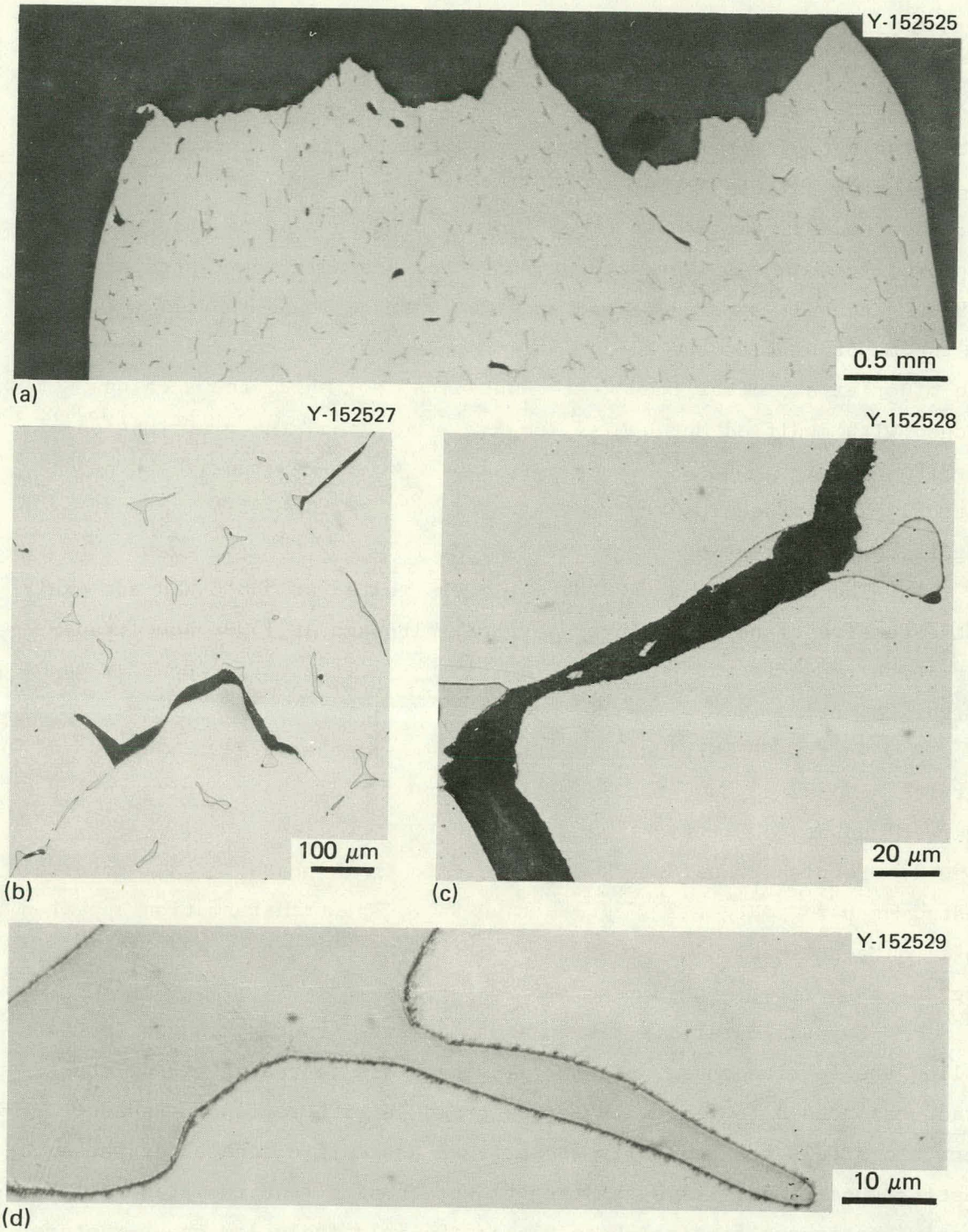

Fig. 28. Specimen of CPF8(L) that Ruptured at 538°C after 102.8 h. (a) Overall view of fracture. (b) Cracks tend to intersect ferrite regions (dark grey phase). (c) Fracture follows paths both through the ferrite phase and very close to the original ferrite-austenite phase boundary, but some evidence of transformation is seen in the vicinity of the original austenite-ferrite phase boundary. (d) Ferrite (dark grey) away from crack essentially untransformed during testing.

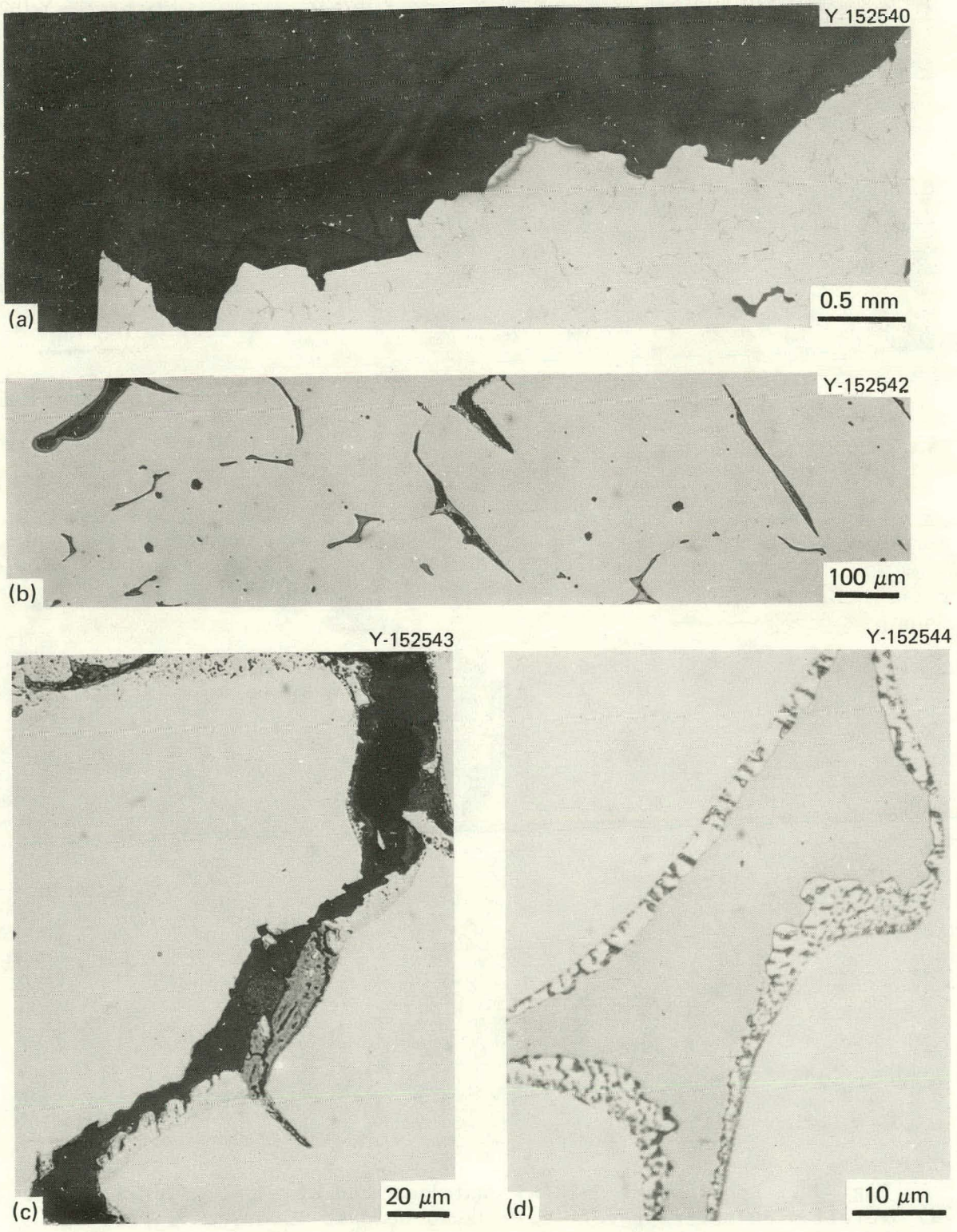

Fig. 29. Specimen of CPF8(L) that Ruptured at 649°C after 167.2 h. (a) Overall view of the fracture region. (b) Cracks tend to follow original ferrite phase. (c) Separations follow the boundary between the untransformed ferrite and the rim of austenite plus sigma formed at the original α-γ boundary. (d) Rim of austenite plus sigma on a ferrite island away from cracks.

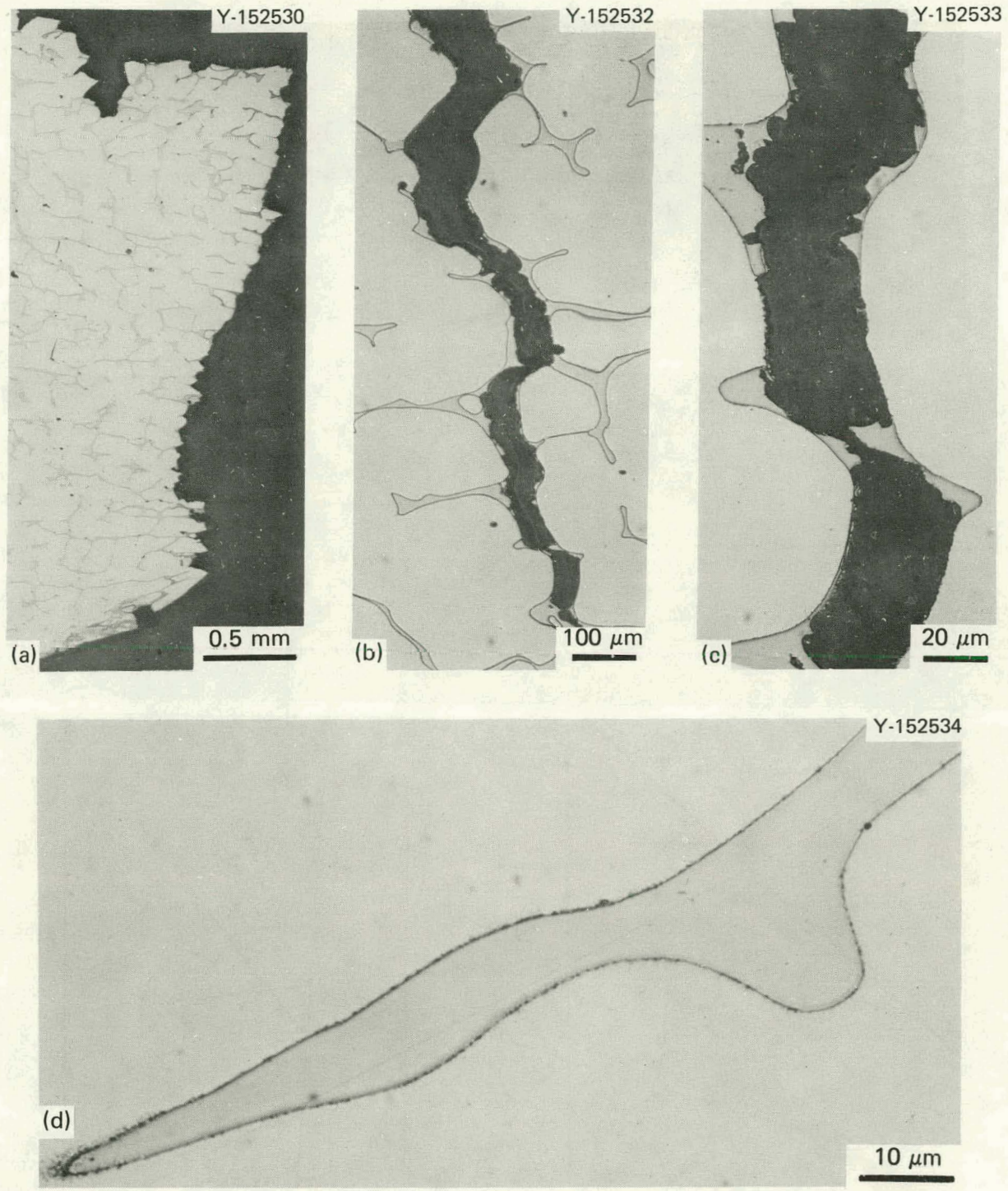

Fig. 30. Specimen of CPF8(H) that Ruptured at 538°C after 58.2 h. (a) Overall view of fracture. (b) Cracks tend to intersect ferrite regions (dark grey). (c) Fracture follows paths both through the ferrite phase and very close to the original ferrite-austenite phase boundary, but some evidence of transformation is seen near the original austenite-ferrite phase boundary. (d) Ferrite (dark grey) essentially untransformed during testing.

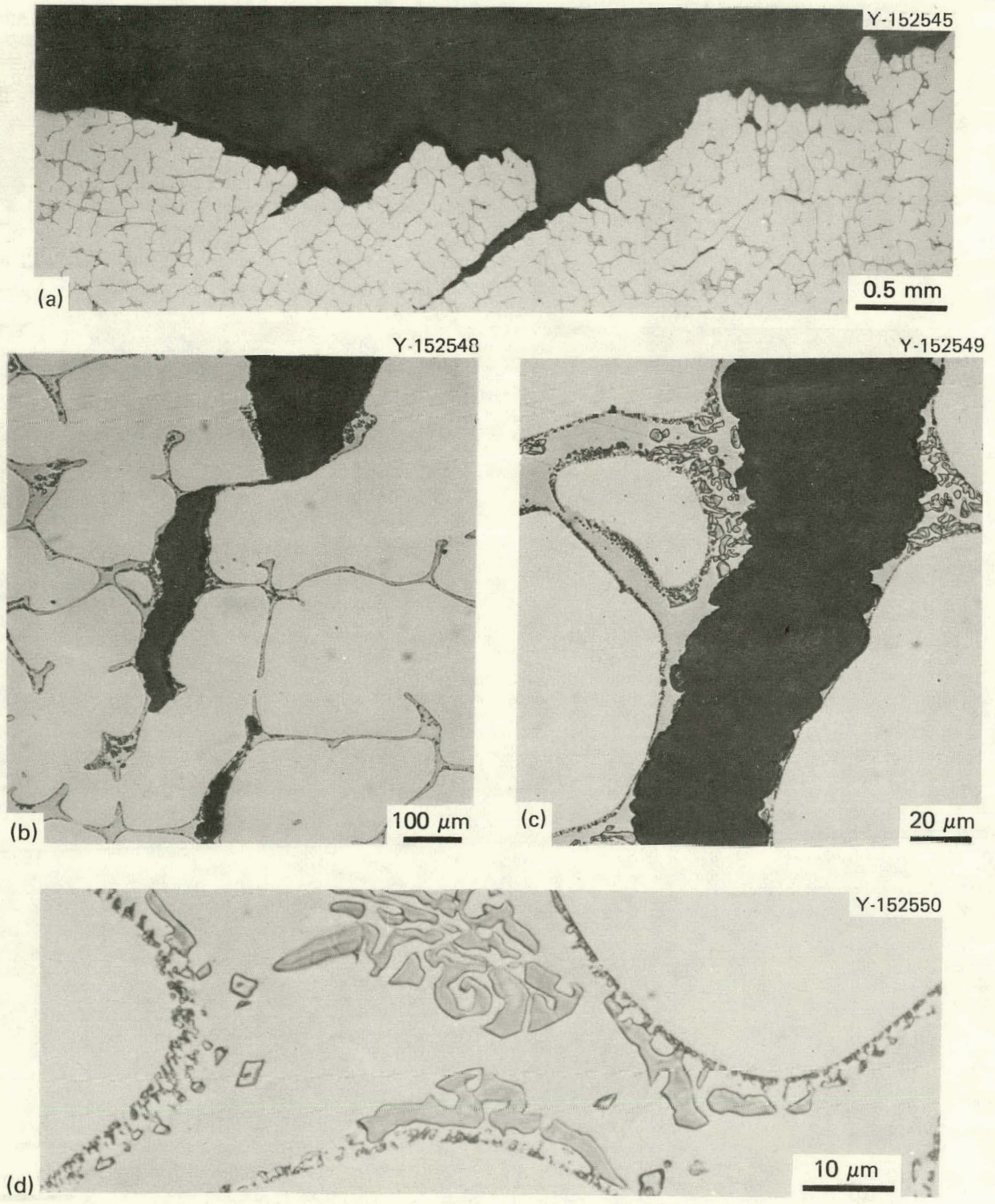

Fig. 31. Specimen of CPF8(H) that Ruptured at 649°C after 407.1 h. (a) Overall view of fracture region. (b) Cracks are almost exclusively in region of original ferrite phase. (c) Fracture clearly occurs in region where ferrite has transformed to austenite and sigma phase. (d) Uncracked region showing both fine sigma phase particles near original austenite-ferrite boundary and more massive sigma phase formed in interior of ferrite phase.

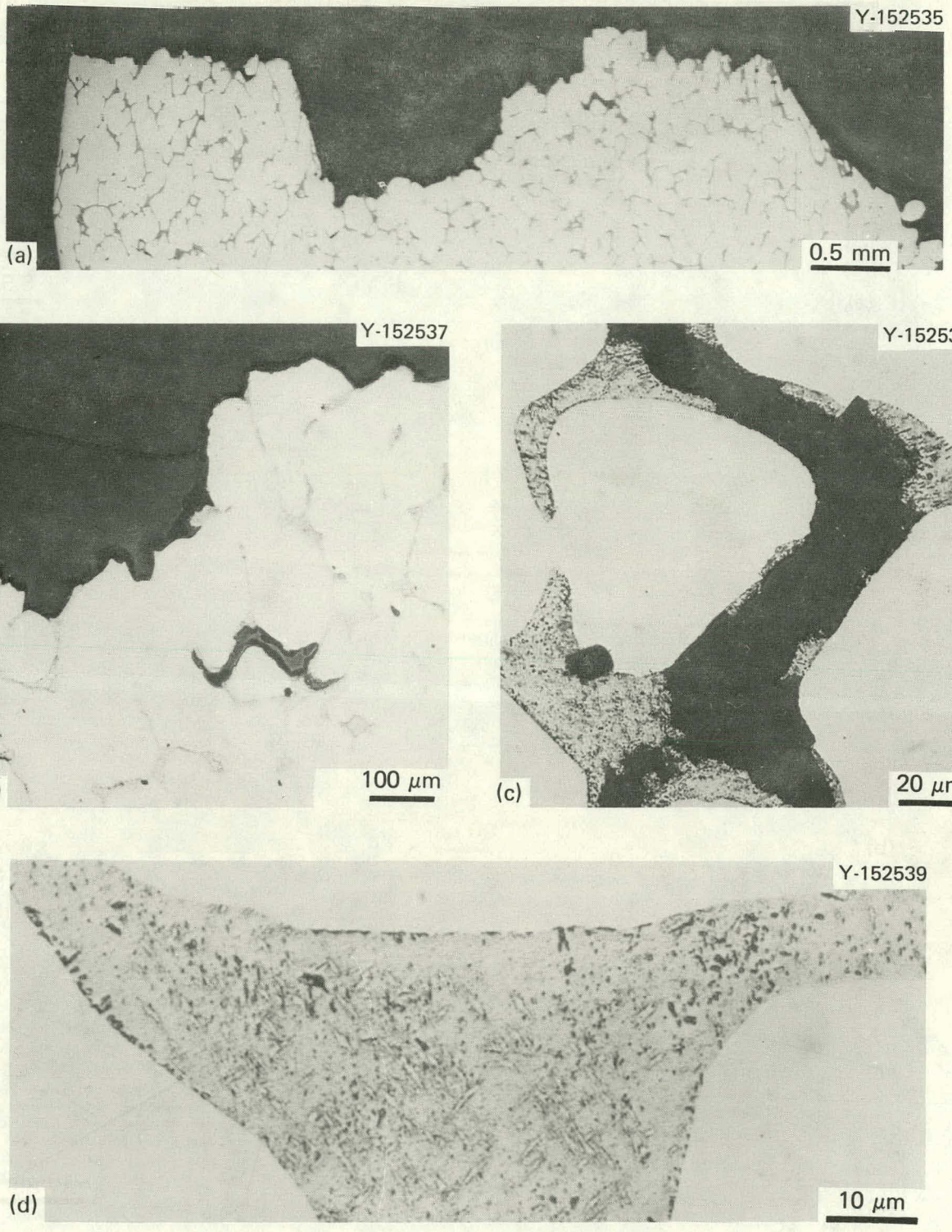

Fig. 32. Specimen of CPF8M(L) that Ruptured at 538°C after 1812.4 h. (a) Overall view of fracture. (b) Cracks tend to follow original ferrite regions. (c) Fracture closely follows original austenite-ferrite phase boundary, crossing from side to side of the ferrite phase. (d) Uncracked region of ferrite showing partial transformation both at original austenite-ferrite boundary and within ferrite.

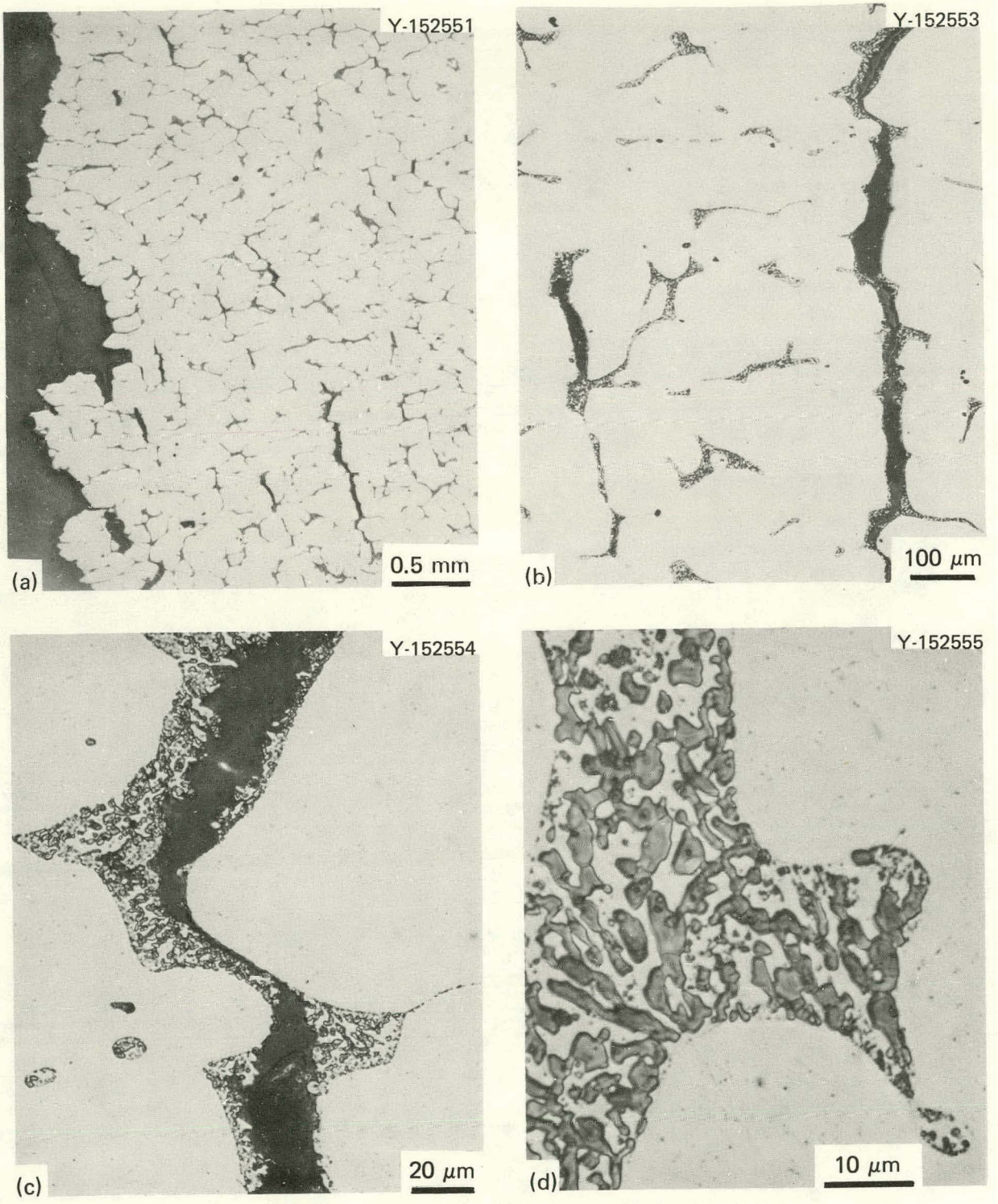

Fig. 33. Specimen of CPF8M(L) that Ruptured at 649°C after 2214.5 h. (a) Overall view of fracture region. (b,c) Cracks tend to follow original ferrite phase region. (d) Uncracked region showing nearly complete transformation of ferrite.

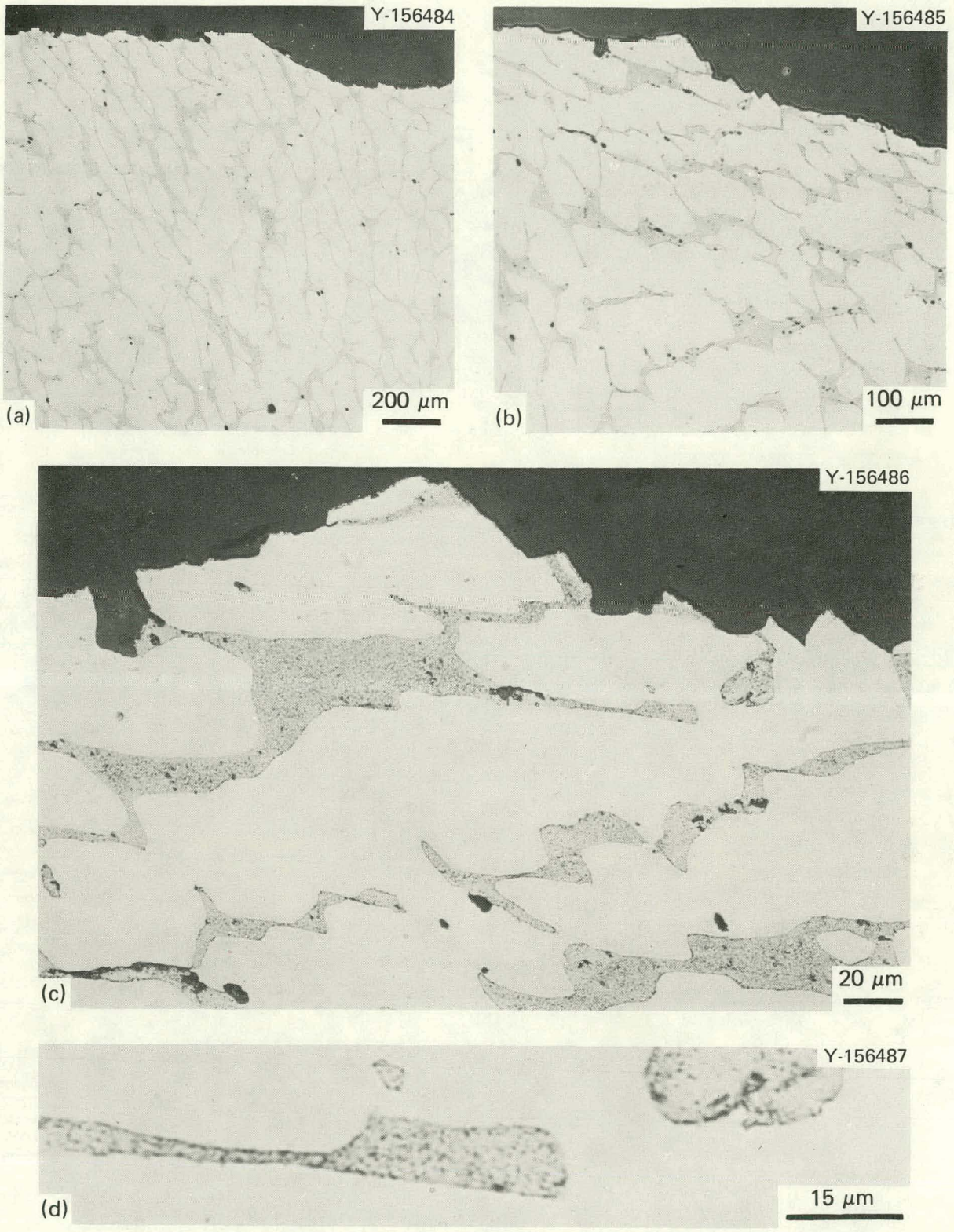

Fig. 34. Specimen of CPF8M(H) that Ruptured at 538°C after 971.4 h. (a) View of fracture region. (b) Cracks tend to follow original ferrite phase region. (c) Same region as b, extensive nucleation of transformation in uncracked ferrite islands.

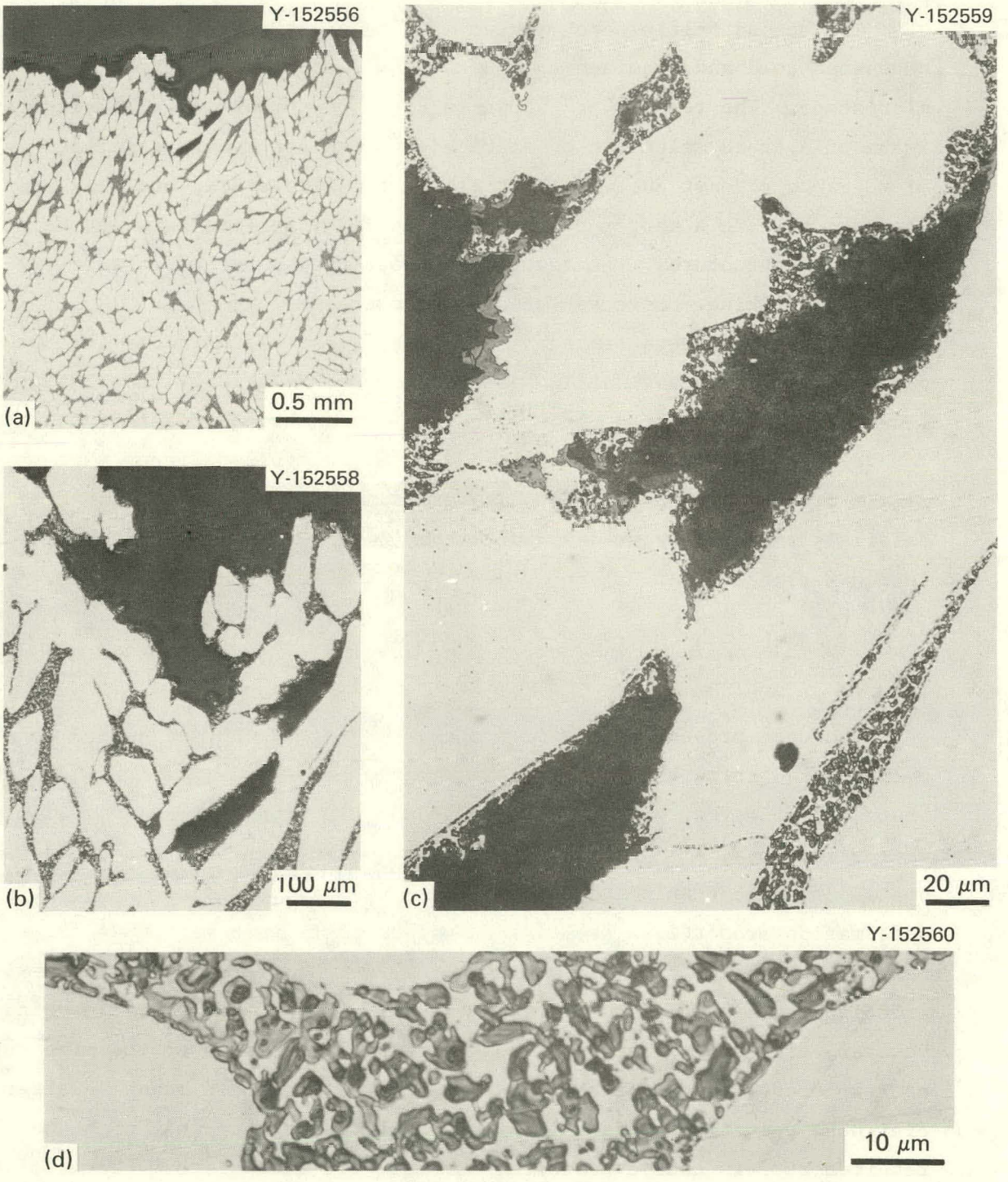

Fig. 35. Specimen of CPF8M(H) that Ruptured at 649°C after 916.3 h. (a) View of fracture region. (b,c) Cracks tend to follow original ferrite region. (d) Uncracked region showing nearly complete transformation of ferrite.

The second half of each tested specimens was plated with vapor-deposited gold and examined on a JOEL-JEM-U3 scanning electron microscope. The results are shown in Figs. 36 through 43. We are not aware of a broad selection of elevated-temperature fracture surface micrographs of cast austenitic steels in the literature, and they are included here as a matter of record. The relationships between the original microstructures, the fracture micrographs, and the fracture surface are striking. Some key observations are:

1. For specimens tested at 538°C, the fracture surfaces that propagate through the austenitic phase tend to be relatively smooth at 1000×, while the ferrite phase tears and forms obvious dimples.

2. For specimens tested at 649°C, the fracture surfaces that propagate through the austenitic phase are somewhat smooth (but the fine detail is obscured by oxide), while the fracture path through the transformed ferrite appears to be affected by the sigma phase particles.

DISCUSSION AND SUMMARY

The data presented above are only a subset of the set needed to properly characterize the centrifugally cast pipes. From the microstructures that were observed, earlier work on austenitic steel welds having similar microstructures,[6,7,9] and measurements reported here for tested specimens one should expect anisotropy of elastic, plastic, and time-dependent deformation properties. Tensile and creep tests were performed for specimens whose tensile axes lie approximately in the direction of the maximum principal stress in a pressurized pipe — the circumferential direction. However, property variations through the wall thickness of the pipe were not explored. No data are shown for pipe that has been annealed after finishing operations. From the standpoint of the data that might be required to gain code acceptance, our data are incomplete in terms of the tensile test temperatures included, creep-rupture test temperatures and times included, and the absence of fatigue data. A significant number of finished tensile samples of other pipe segments are available for further testing, but data from other castings will undoubtedly be needed for further testing for acceptance.

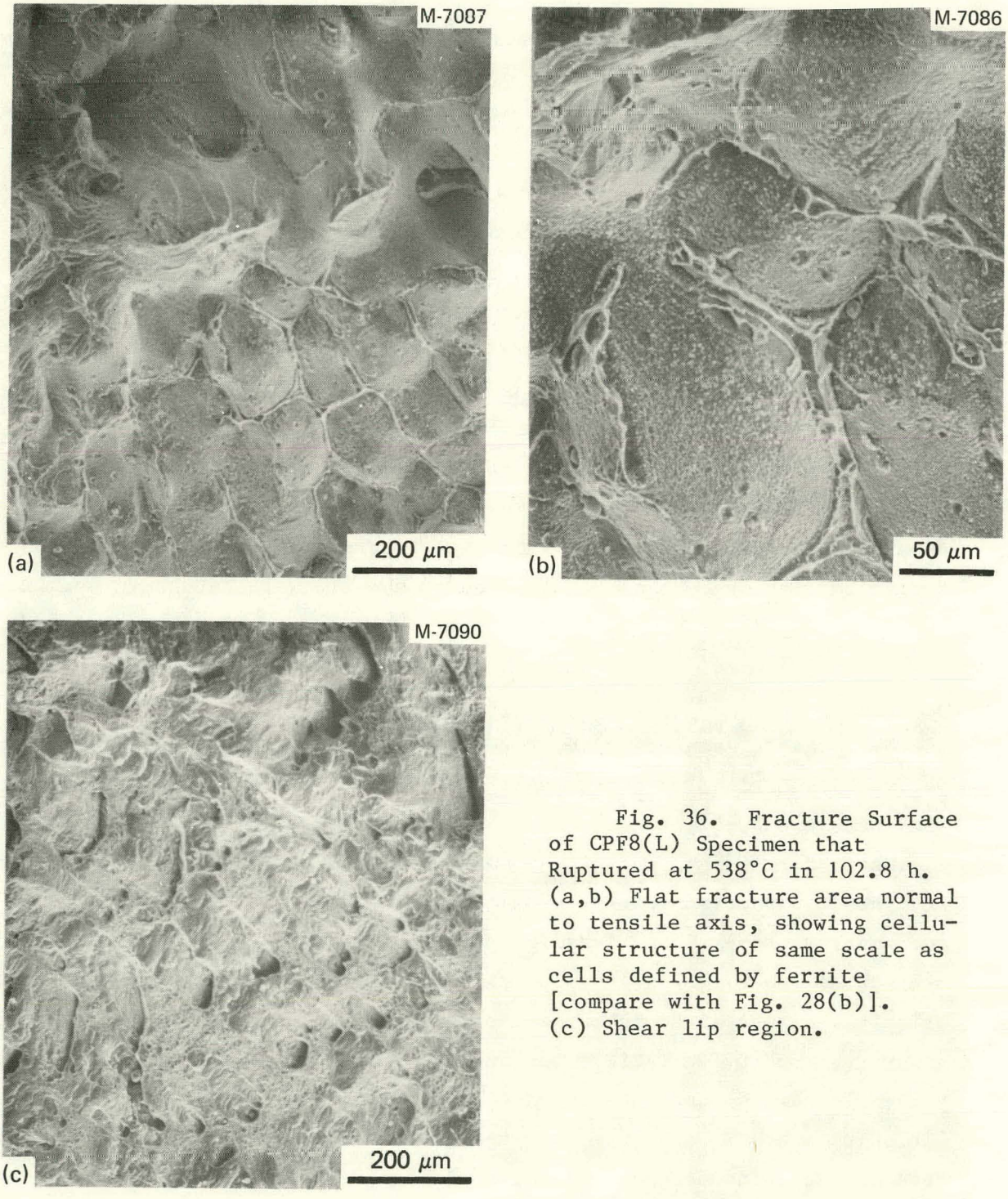

Fig. 36. Fracture Surface of CPF8(L) Specimen that Ruptured at 538°C in 102.8 h. (a,b) Flat fracture area normal to tensile axis, showing cellular structure of same scale as cells defined by ferrite [compare with Fig. 28(b)]. (c) Shear lip region.

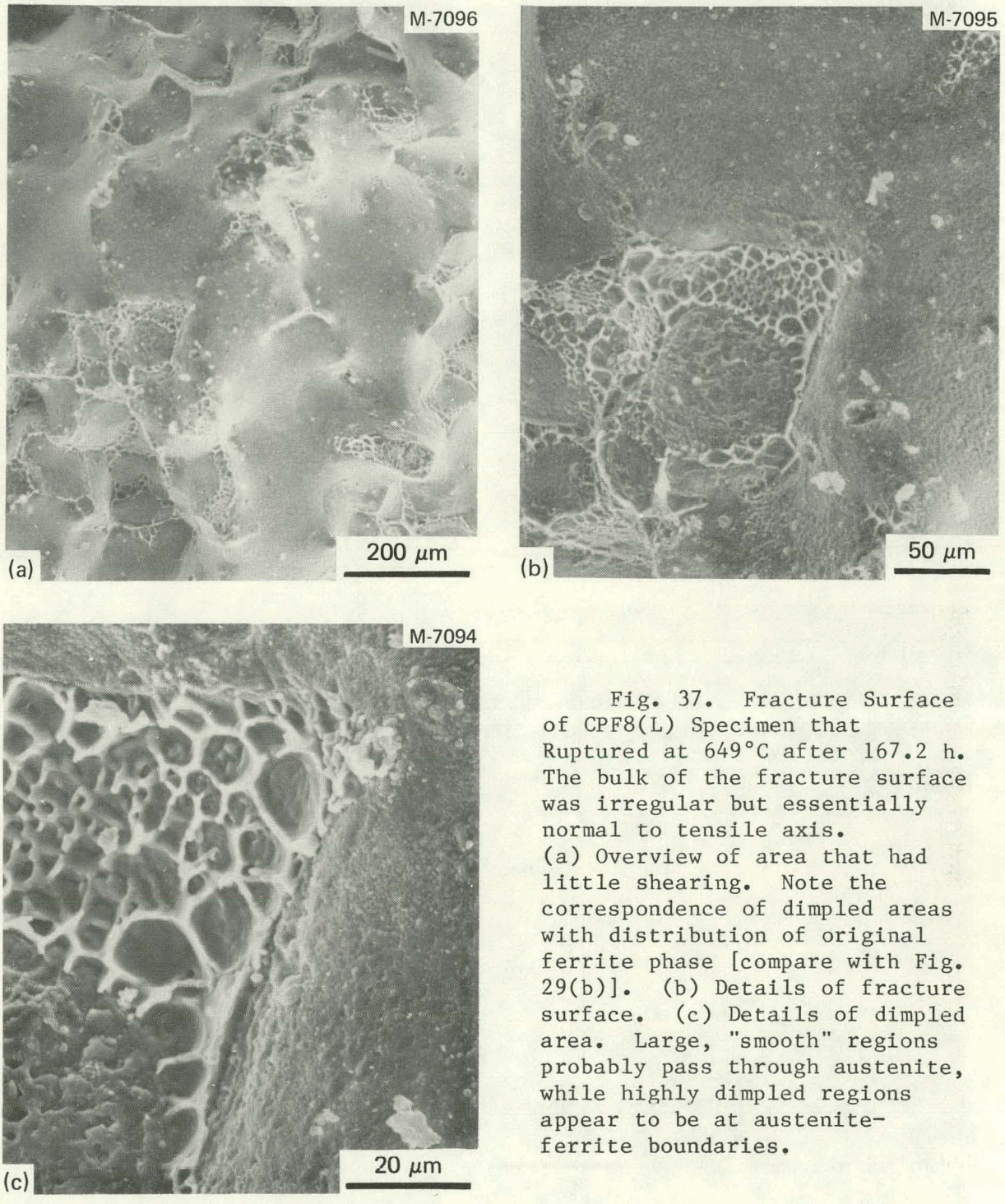

Fig. 37. Fracture Surface of CPF8(L) Specimen that Ruptured at 649°C after 167.2 h. The bulk of the fracture surface was irregular but essentially normal to tensile axis. (a) Overview of area that had little shearing. Note the correspondence of dimpled areas with distribution of original ferrite phase [compare with Fig. 29(b)]. (b) Details of fracture surface. (c) Details of dimpled area. Large, "smooth" regions probably pass through austenite, while highly dimpled regions appear to be at austenite-ferrite boundaries.

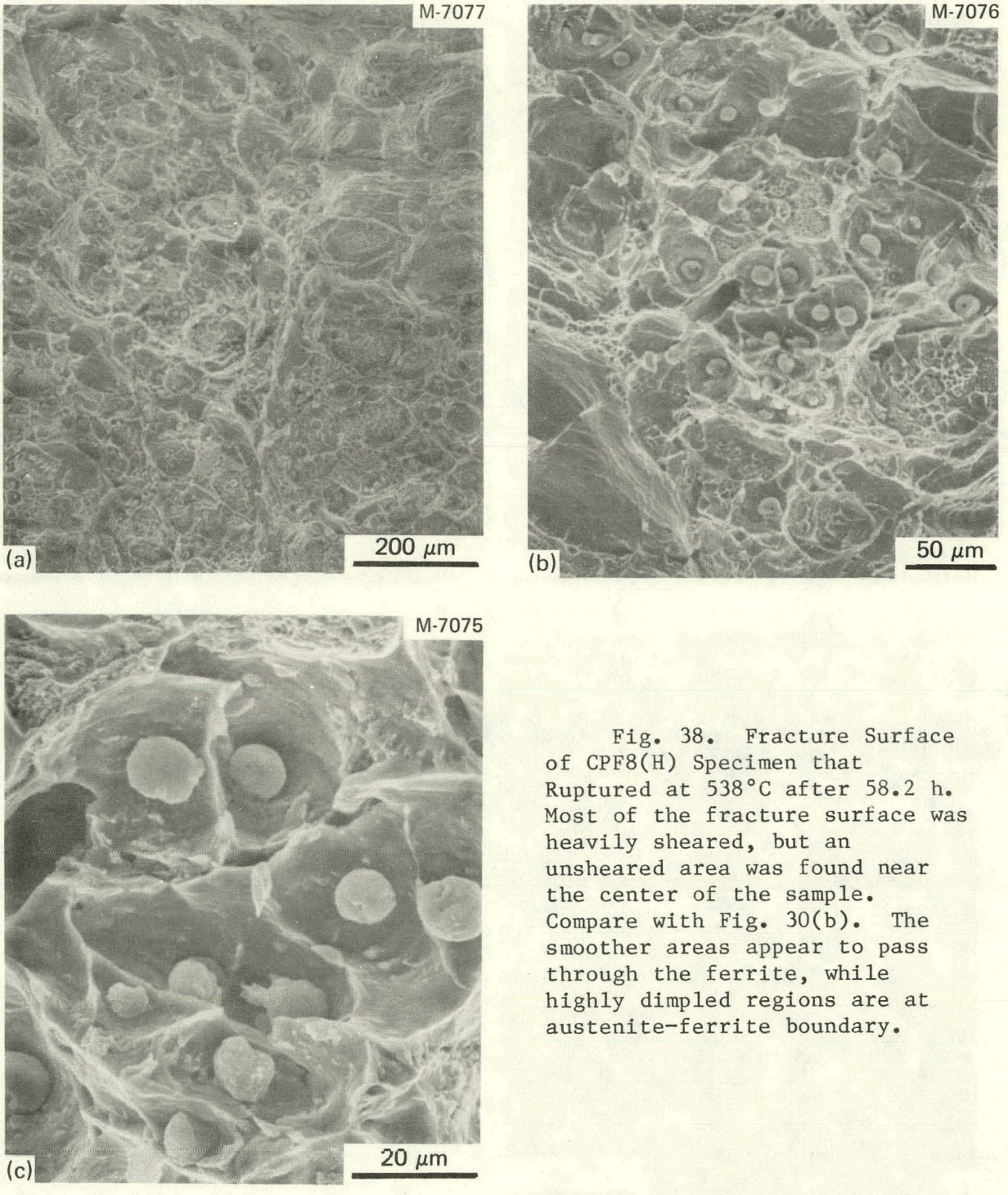

Fig. 38. Fracture Surface of CPF8(H) Specimen that Ruptured at 538°C after 58.2 h. Most of the fracture surface was heavily sheared, but an unsheared area was found near the center of the sample. Compare with Fig. 30(b). The smoother areas appear to pass through the ferrite, while highly dimpled regions are at austenite-ferrite boundary.

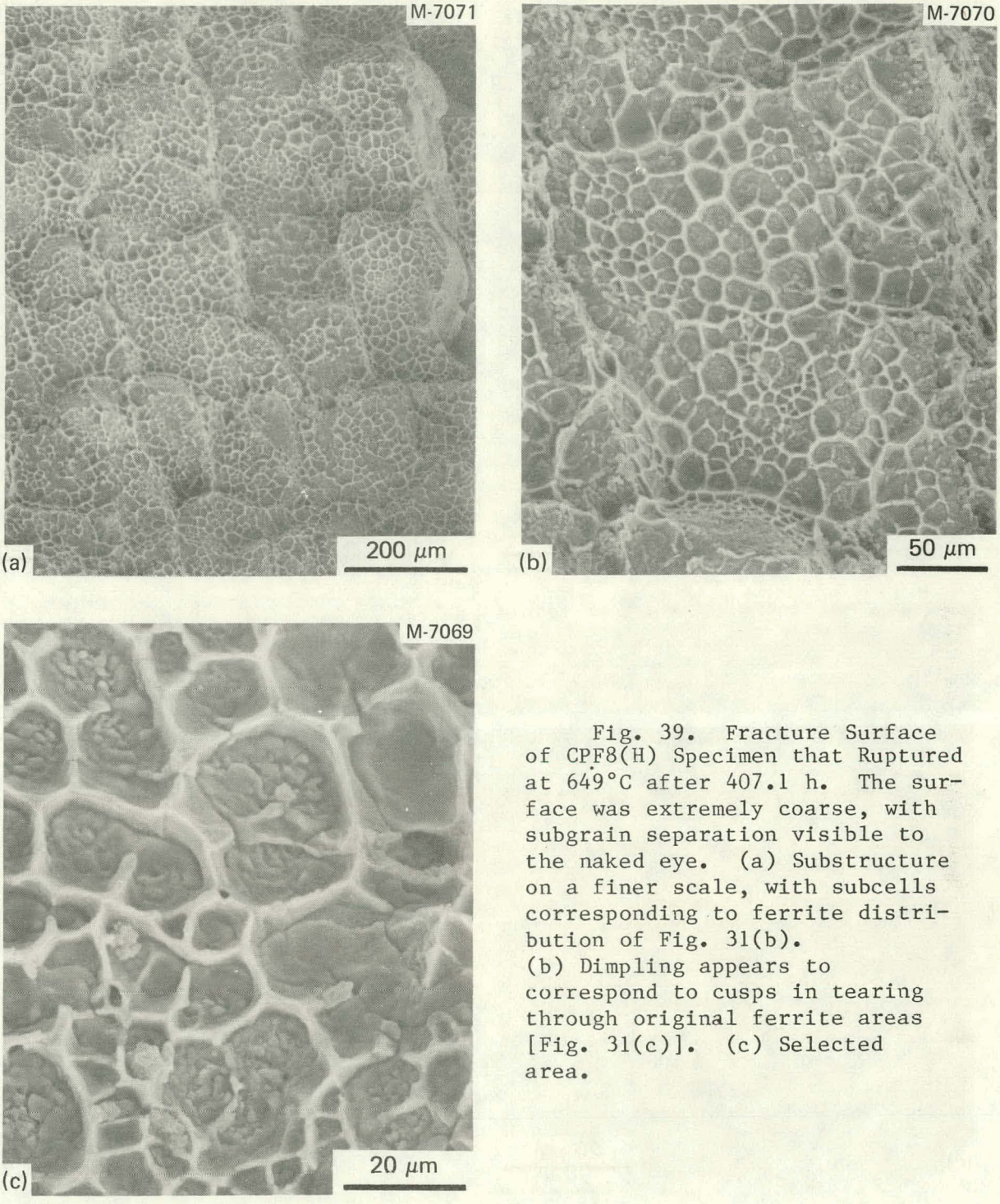

Fig. 39. Fracture Surface of CPF8(H) Specimen that Ruptured at 649°C after 407.1 h. The surface was extremely coarse, with subgrain separation visible to the naked eye. (a) Substructure on a finer scale, with subcells corresponding to ferrite distribution of Fig. 31(b). (b) Dimpling appears to correspond to cusps in tearing through original ferrite areas [Fig. 31(c)]. (c) Selected area.

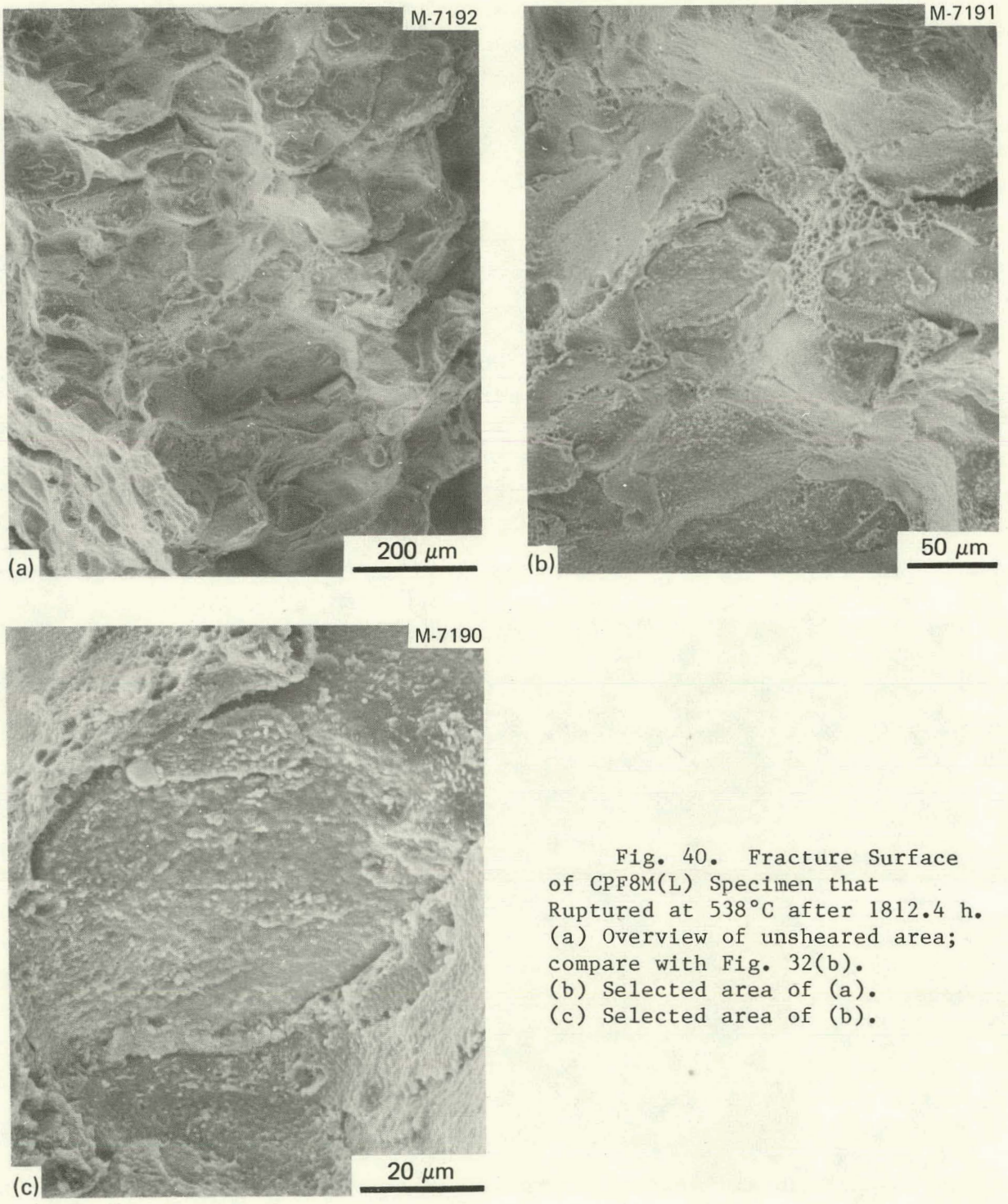

Fig. 40. Fracture Surface of CPF8M(L) Specimen that Ruptured at 538°C after 1812.4 h.
(a) Overview of unsheared area; compare with Fig. 32(b).
(b) Selected area of (a).
(c) Selected area of (b).

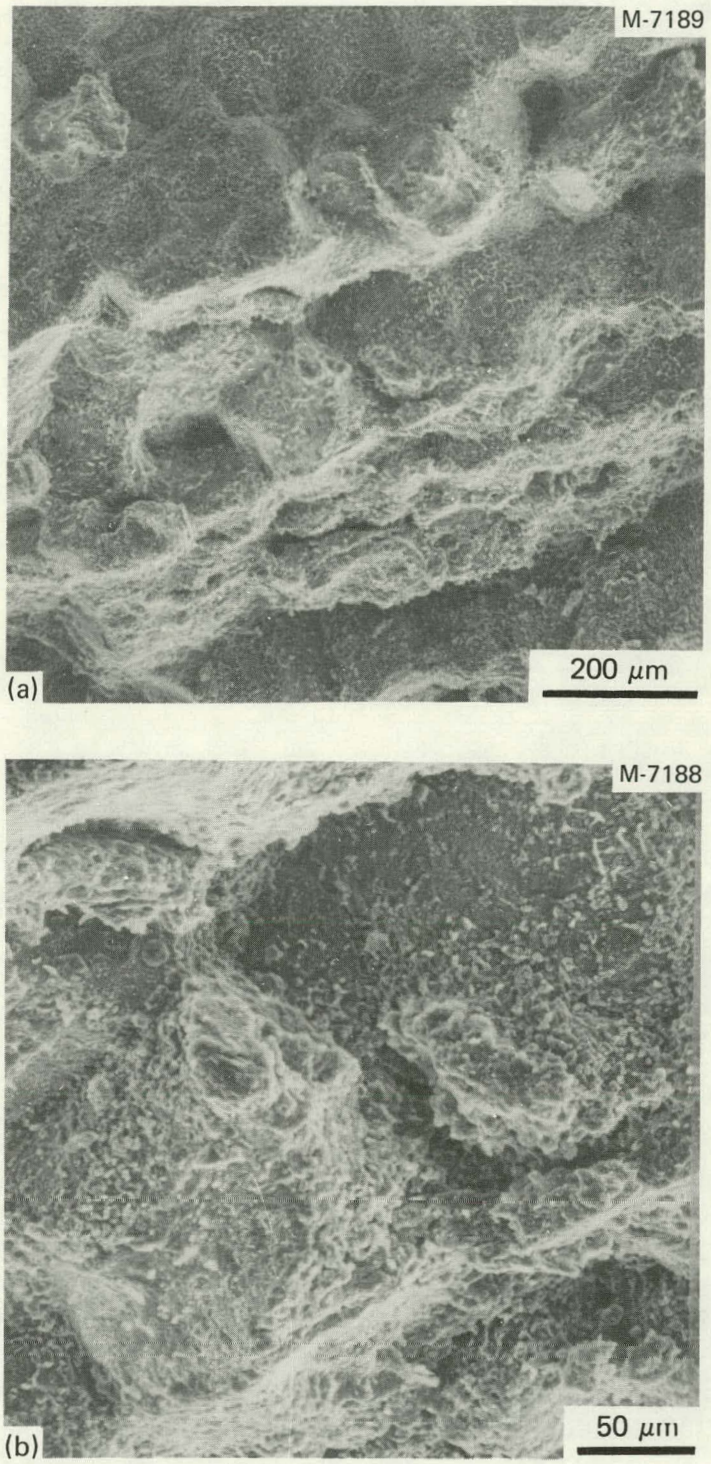

Fig. 41. Fracture Surface of CPF8(L) Specimen that Ruptured at 649°C after 2214.5 h. A coarse subgrain structure normal to the tensile axis was visible to the naked eye. (a) Fracture surface is related to original ferrite distribution [see Fig. 33(b)]. (b) Roughness of fracture surface is probably related to sigma phase distribution in transformed ferrite [see Fig. 33(c,d)].

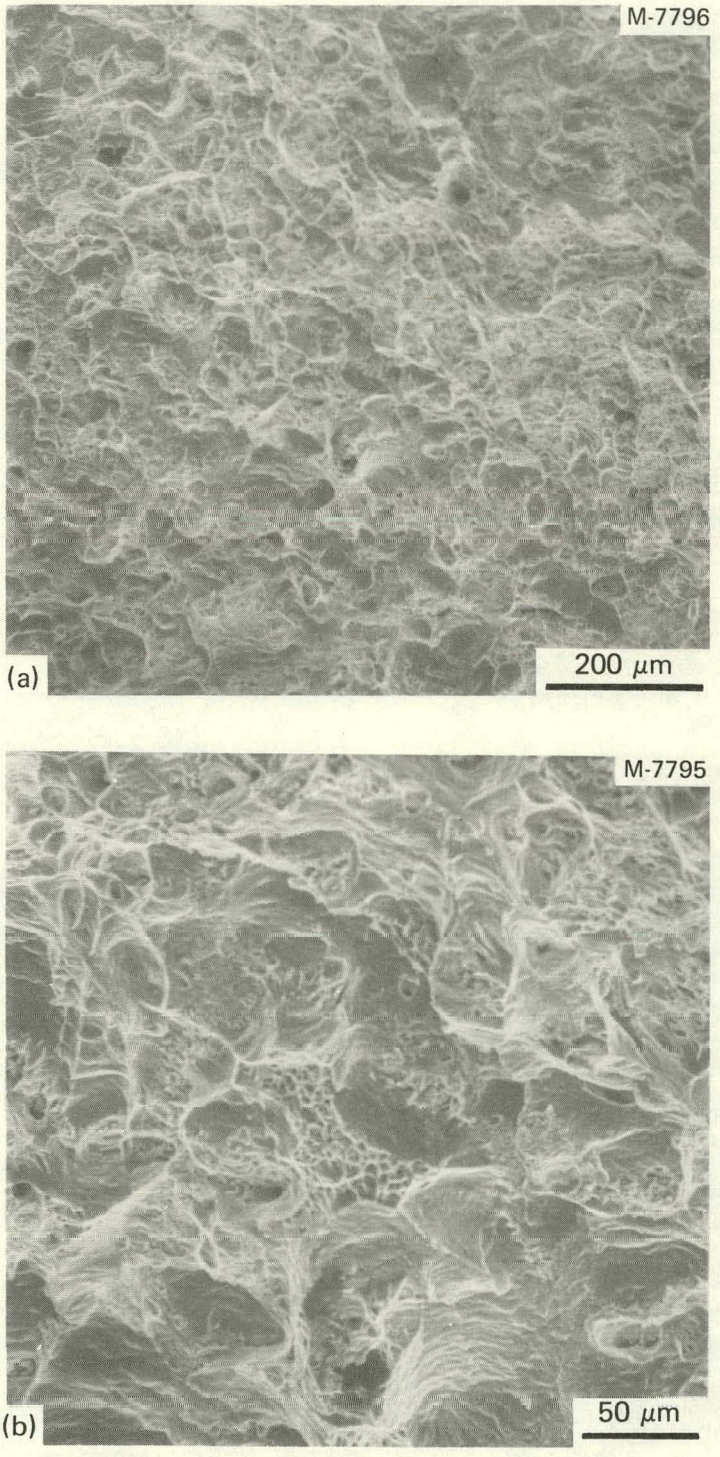

Fig. 42. Fracture Surface of CPF8M(H) Specimen that Ruptured at 538°C after 971.4 h.

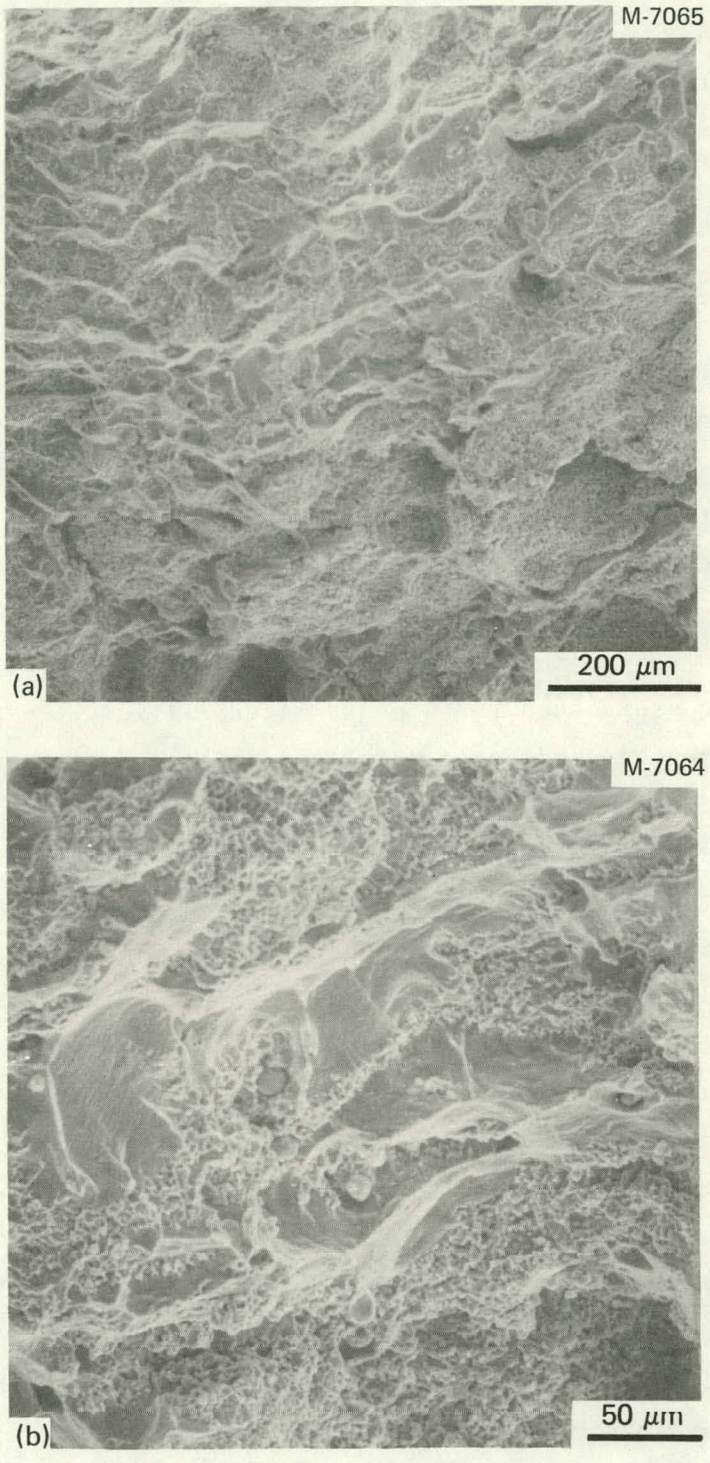

Fig. 43. Fracture Surface of CPF8M(H) Specimen that Ruptured at 649°C after 916.3 h. A small shear lip area was not photographed. (a) Overview comparable to Fig. 35(b). (b) Selected area showing rough surface in transformed regions; sheared areas thought to be austenite.

The data that are available for wrought austenitic steels exhibit scatter, some of which is attributed to variations of chemical contents within specification limits, to variations in microstructure resulting from variations in processing history, and to variations in residual cold work resulting from straightening or finishing operations. While processing history is not a variable in castings, the chemical contents, melting and casting practice, mold configuration, and annealing treatments can all affect the microstructure and hence the properties of austenitic stainless steel castings. A base of data is needed to account for these potentially important factors.

We will not compare these data with those available in the literature for other CPF8 and CPF8M castings; a separate review report on that topic is in preparation.

Comparisons of the tensile and creep-rupture properties of the cast steels with those suggested for wrought material yield the following points that suggest a need for careful comparison of cast and wrought material properties:

1. The yield and ultimate tensile strengths of low-ferrite-bearing CPF8 are lower than minimum properties suggested for wrought materials.

2. The ultimate tensile strengths of all CPF8 and CPF8M castings tested at 538 and 649°C were lower than the minimum values suggested for wrought materials.

3. The measured creep-rupture strengths at 538 and 649°C of cast CPF8 and CPF8M are well below the "average" values reported for multiple heats of their wrought counterparts, and they frequently have shorter rupture times than the "minimum" values suggested for their wrought counterparts, types 304 and 316 stainless steel.

4. In addition, the creep ductility of CPF8 appears to decrease significantly with rupture time at both 538 and 649°C. Both CPF8 and CPF8M material exhibit creep fracture morphologies that are similar to those sometimes associated with low creep ductility and sigma phase formation in austenitic stainless steel welds.[6] The lowest total creep rupture strains measured were 6.9 and 16.6% for CPF8 and CPF8M, respectively, for tests lasting between 100 and 1000 h.

These findings suggest strongly that the property data for cast and wrought austenitic steels of similar compositions should not be grouped for design purposes. None of these data preclude the safe use of these materials under suitable design rules.

ACKNOWLEDGMENTS

The authors thank Warren P. Stubblebine of Sandusky Foundary and Machine Company, Sandusky, Ohio, for supplying the experimental material and for helpful suggestions during the course of the work. We also thank W. A. House and R. A. Nation of Combustion Engineering, Chattanooga, Tennessee, who performed certain chemical analyses, and J. P. Hammond of ORNL for tensile curves at low temperatures. We are grateful to C. W. Houck and T. J. Henson for the metallographic work and the scanning electron microscopy, respectively. The support and encouragement of P. Patriarca of ORNL and E. E. Hoffman of the Division of Reactor Research and Technology, Department of Energy, are gratefully acknowledged. We wish to thank S. Peterson for the final editorial work and P. T. Thornton of the Metals and Ceramics Division Reports Office for preparing the final manuscript.

REFERENCES

1. *ASME Boiler and Pressure Vessel Code*, Sect. III, American Society of Mechanical Engineers, New York, 1977, Table I-1.2
2. Ibid., footnote to Table I-7.2, for example.
3. (Personal Communication) W. P. Stubblebine, Sandusky Foundary and Machine Company, Sandusky, Ohio, 1976.
4. C. R. Brinkman, V. K. Sikka, and R. T. King, *Mechanical Properties of LMFBR Primary Piping Materials*, ORNL-5199 (November 1976).
5. J. O. Steigler, R. T. King, and G. M. Goodwin, "Effect of Residual Elements on Fracture Characteristics and Creep Ductility of Type 308 Stainless Steel Weld Metal," *J. Eng. Mater. Technol.* 97: 245–50 (July 1975).

6. B. R. Dewey, L. Adler, R. T. King, and K. V. Cook, "Measurements of Anisotropic Elastic Constants of Type 308 Stainless-Steel Electroslag Welds," *Exp. Mech.* 17(11): 420–26 (November 1977).
7. J. W. McEnerney, "Piping and Fittings," *Breeder Reactor Materials Development Program Quart. Prog. Rep. June 30, 1977*, ORNL-5359, pp. 109–78.
8. B. R. Dewey, L. Adler, R. T. King, and K. V. Cook, *Application of Anisotropic Elasticity to Centrifugally Cast Piping*, ORNL/TM-5994 (October 1977).
9. B. R. Dewey, private communication based on unpublished data, 1977.
10. *ASME Boiler and Pressure Vessel Code*, Sect. III, American Society of Mechanical Engineers, New York, 1977, Fig. NB-2433.1-1, p. 21.
11. *Nuclear Systems Materials Handbook, Vol. 1, Design Data*, TID-26666, Hanford Engineering Development Laboratory, Richland, Washington, Values available as of July 1978.
12. J. W. McEnerney and V. K. Sikka, *Characterization of Three Developmental Centrifugally Cast and Worked Austenitic Stainless Steel Pipes, Part II*. (Report in preparation).
13. D. O. Hobson and T. L. Hebble, "Statistical Analysis of Type 304 Stainless Steel Creep-Rupture Data," *Mechanical Properties Test Data for Structural Materials Quart. Prog. Rep. Oct. 31, 1973*, ORNL-4936, pp. 111 17.
14. L. D. Blackburn, "Isochronous Stress-Strain Curves for Austenitic Stainless Steels," pp. 15–48 in *The Generation of Isochronous Stress-Strain Curves*, A. O. Schaefer, Ed., American Society of Mechanical Engineers, New York, 1972.
15. R. J. Gray, R. S. Crouse, V. K. Sikka, and R. T. King, "A Metallographic Study of Ferrite-Sigma Phase Transformation using Ferromagnetic Colloid, Microprobe Analysis, and Color Etching," pp. 65–84 in *Microstructural Science*, Vol. 5, Elsevier, New York, 1977.

ORNL/TM-7142
Distribution
Categories UC-79h,
-k, -r

INTERNAL DISTRIBUTION

1–2. Central Research Library
3. Document Reference Section
4–5. Laboratory Records Department
6. Laboratory Records, ORNL RC
7. ORNL Patent Section
8–10. E. Bolling
11. M. K. Booker
12. C. R. Brinkman
13. J. M. Corum
14. B. R. Dewey
15. G. M. Goodwin
16. R. J. Gray
17–19. M. R. Hill
20. R. L. Klueh
21. W. J. McAfee
22. J. W. McEnerney
23. C. E. Pugh
24–38. V. K. Sikka
39. G. M. Slaughter
40. R. W. Swindeman
41. A. L. Bement, Jr. (Consultant)
42. W. R. Hibbard, Jr. (Consultant)
43. E. H. Kottcamp, Jr. (Consultant)
44. M. J. Mayfield (Consultant)
45. J. T. Stringer (Consultant)

EXTERNAL DISTRIBUTION

46. DOE, DIVISION OF REACTOR RESEARCH AND TECHNOLOGY,
Washington, DC 20545

Director

47. DOE, OAK RIDGE OPERATIONS OFFICE, P.O. Box E, Oak Ridge, TN 37830

Office of Assistant Manager, Energy Research and Development

48-249. DOE, TECHNICAL INFORMATION CENTER, P.O. Box 62, Oak Ridge, TN 37830

For distribution shown in TID-4500 Distribution Category,
UC-79h, (Structural Materials and Design Engineering);
UC-79k, (Components); and UC-79r, (Structural and Component
Materials Development).

U.S. GOVERNMENT PRINTING OFFICE: 1980-640-245-436